

Small polarons mediated near-room-temperature metal-insulator transition in vanadium dioxide and their hopping dynamics

<https://doi.org/10.1063/5.0236807>

Xiongfang Liu^{1,#}, Tong Yang^{2,#}, Shanquan Chen^{3,#}, Jing Wu⁴, Chi Sin Tang^{1,5,}, Yuanjie Ning¹, Zuhuang Chen³, Liang Dai¹, Mengxia Sun¹, Mingyao Chen¹, Kun Han⁶, Difan Zhou¹, Shengwei Zeng⁴, Shuo Sun¹, Sensen Li⁷, Ming Yang^{2,*}, Mark B. H. Breese^{5,8}, Chuanbing Cai¹, Thirumalai Venkatesan⁹, Andrew T. S. Wee^{8,10}, Xinmao Yin^{1,*}*

¹Shanghai Key Laboratory of High Temperature Superconductors, Institute for Quantum Science and Technology, Department of Physics, Shanghai University, Shanghai 200444, China

²Department of Applied Physics, The Hong Kong Polytechnic University, Kowloon, Hong Kong, 100872, China

³School of Materials Science and Engineering Harbin Institute of Technology, Shenzhen 518055, China

⁴Institute of Materials Research and Engineering (IMRE), Agency for Science, Technology and Research (A*STAR), 2 Fusionopolis Way, Innovis #08-03, Singapore 138634, Singapore

⁵Singapore Synchrotron Light Source (SSLS), National University of Singapore, Singapore 117603, Singapore

⁶Information Materials and Intelligent Sensing Laboratory of Anhui Province, Institutes of Physical Science and Information Technology, Anhui University, Hefei 230601, China

⁷Department of Electronic Engineering, School of Electronic Science and Engineering, Xiamen University, Xiamen 361005, China

⁸Department of Physics, Faculty of Science, National University of Singapore, Singapore 117542, Singapore

⁹Center for Quantum Research and Technology, University of Oklahoma, Norman, Oklahoma 73019, USA

¹⁰Centre for Advanced 2D Materials and Graphene Research, National University of Singapore, Singapore 117546, Singapore

#These authors contributed equally to this work.

*Corresponding author: slscst@nus.edu.sg (C.S.T.); kevin.m.yang@polyu.edu.hk (M.Y.); yinxinmao@shu.edu.cn (X.Y.)

ABSTRACT

Researchers pursuing advanced photoelectric devices have discovered near room-temperature metal-insulator transitions (MIT) in non-volatile VO₂. Despite theoretical investigations suggesting that polaron dynamics mediate the MIT, direct experimental evidence remains scarce. In this study, we present direct evidence of the polaron state in insulating VO₂ through high-resolution spectroscopic ellipsometry measurements and first-principles calculations. We illustrate the complementary role of polaron dynamics in facilitating Peierls and Mott transitions, thereby contributing to the MIT processes. Furthermore, our observations and characterizations of conventional metallic and correlated plasmons in the respective phases of the VO₂ film offer valuable insights into their electron structures. This investigation enhances comprehension of the MIT mechanism in correlated systems and underscores the roles of polarons, lattice distortions, and electron correlations in facilitating phase transition processes in strongly-correlated systems. Additionally, the detailed detection of small polarons and plasmons serves as inspiration for the development of new device functionalities.

KEYWORDS

polarons; plasmon; electron structures; first-principles calculations; room-temperature metal-insulator transition

I. INTRODUCTION

Strongly-correlated electron systems take centerstage in Condensed Matter Physics where the investigation of quantum many-body effects coupled with charge, orbital, spin and lattice degrees of freedom give rise to a rich family of nontrivial critical phenomena such as high-temperature superconductivity (1, 2), charge-density wave order (3, 4) and pair-density wave order (5, 6). Specifically, metal-insulator transition (MIT) phenomenon in Mott insulators emerges as a quintessential feature amongst various quantum mechanical effects (7). The MIT phenomenon can be manipulated via multiple approaches including carrier density modulation, orbital occupancy and photo-induction (8-10). As such, the high-tunable MIT properties enable a diverse range of quantum materials to be utilized in multiple applications related to energy-efficient systems (11), neuromorphic devices (9) and radiative thermal memristors (12). While

the prospects of a diverse range of applications have been promising, complex strongly-correlated electronic systems still present a challenge especially in the attempt to identify the underlying physical mechanism governing the MIT processes, which to date, remains to be understood.

Vanadium dioxide (VO_2) serves as an ideal platform for the detailed investigation of MIT properties. As an archetypical non-volatile Mott insulator, VO_2 has long captivated researchers due to the intriguing MIT process taking place near room temperature ($T \approx 68 \text{ }^\circ\text{C}$). The room-temperature MIT process accords VO_2 with potential for practical applications in areas such as the energy sectors, smart windows technology and neuromorphic sensors (9, 11, 13). This first-order phase transition is marked by an abrupt increase in electrical resistivity by several orders of magnitude from a metallic state at high temperature to an insulating state at low temperature. Concomitant with this electronic transition is a structural transition, where the crystal lattice shifts from the high-temperature rutile phase to the low-temperature monoclinic phase. The monoclinic structure is distinguished by the dimerization of vanadium atoms and a tilting relative to the c -axis, a feature that has been closely associated with the insulating state (14). However, the underlying mechanism driving this MIT remains a matter of extensive debate, centering on whether the structural transition or the electronic correlations which takes precedence.

Over the decades, various theoretical frameworks have emerged to explain the MIT process in VO_2 . Initially, the transition was attributed to a Peierls mechanism, wherein the lattice distortions in the monoclinic phase result in a gap opening at the Fermi level, thereby being stabilized in the insulating phase (15). This perspective was supported by early studies that observed the non-magnetic nature of the monoclinic phase, which is consistent with a typical Peierls insulator (7). However, as more advanced experimental techniques, such as the X-ray absorption spectroscopy and angle-resolved photoemission spectroscopy were used to probe the system (16, 17), it became clear that this lattice-centric view does not fully account for the complexity of the mechanism governing the MIT process.

A competing explanation based on electron-electron interactions, known as the Mott mechanism, posits that strong electronic correlations are the primary driver of the transition, with the lattice distortions playing a secondary role (18). Key experimental findings, such as those by Qazilbash *et al.*, highlighted that in the metallic phase, electron-electron interactions dominate the electronic behavior instead of electron-phonon interactions (19). This suggested that VO_2 could undergo a Mott transition, similar to other strongly-correlated electron materials, where insulating behavior emerges due to strong Coulomb repulsion between electrons, independent of any structural phase transition (20, 21). The Mott picture has been bolstered by advances in dynamical mean-field theory (DMFT), which provides a framework for understanding correlated electrons in transition metal oxides (22).

In later years, a growing consensus has emerged that neither the Peierls nor Mott mechanisms alone can comprehensively explain the MIT in VO₂. Instead, a cooperative Peierls-Mott transition is increasingly viewed as the most plausible scenario, where both electron-lattice interactions and electron-electron correlations are essential (23, 24). In this hybrid model, the orbital-selective nature of the Mott transition works in tandem with lattice symmetry breaking to stabilize the insulating phase, providing a more holistic understanding of the transition. This model captures the complex coupling between the electronic and structural degrees of freedom, offering insights into the subtle balance of forces governing the phase change in VO₂.

Despite these advances, significant challenges remain in fully elucidating the mechanism behind the MIT in VO₂. A major limitation lies in disentangling the respective roles of lattice distortions and electronic correlations, as both phenomena are tightly interwoven in the material's phase behavior. With the above consideration, the emergence of polarons (25), a quantum quasiparticle that arises from the coupling between the excess charges and the crystal lattice in strongly-correlated system is the cornerstone to unlock the fundamental understanding of multiple quantum phenomena (26).

The theoretical understanding of polarons began in 1933 with Landau, who suggested that charge carriers could cause local lattice deformation (27). Pekar further formalized this concept by defining the polaron as a quasiparticle resulting from the coupling of a charge with lattice vibrations (28). Two major types of polarons emerged from this work: large polarons, described by Herbert Fröhlich, and small polarons, introduced by Theodore Holstein. Fröhlich's theory applies to polarons with long-range interactions, while Holstein's model focuses on localized, short-range electron-phonon coupling (29).

Over the decades, these theoretical frameworks have expanded, leading to significant developments in both understanding and observing polaron effects. Early models set the foundation for ongoing research, exploring not only single-polaron systems but also complex interactions like bipolarons, magnetic polarons and interfacial polarons (30-33). Experimental breakthroughs, such as optical pump-terahertz probe spectroscopy, Fourier infrared transform spectrometer and soft-X-ray angle-resolved photoelectron spectroscopy (34-36), have further confirmed polaron behavior across a range of materials, including oxides, semimetal, hybrid perovskites and two-dimension interface.

Given the strong influence of charge-lattice coupling, the onset of MIT and its underlying mechanism may fundamentally be mediated by the system's polaron dynamics (30, 37). Besides, polarons are ubiquitous in a diverse range of transition metal oxides (25). Their ability to induce drastic changes, which in turn drives and regulates the corresponding structural and electronic phase transition processes are notable. Notably, extensive computation-led theoretical predictions have been made that point to the prominent existence of small polaron features in VO₂ systems, which originate from the short-range coupling between excess charges and the lattice, along

with their possible influence on its MIT properties (38-40). Thus, an in-depth investigation on how polaron dynamics would be an effective strategy to unlock the MIT mechanism in multiple condensed matter systems. However, a detailed understanding and direct experimental evidence of MIT effects induced by small polarons in VO₂ system remain largely elusive.

Here, we report the observation of a mid-gap state that is present exclusively in the insulating phase of VO₂ on TiO₂(001) substrate. Based on a comprehensive approach that combines temperature-dependent high-resolution spectroscopic ellipsometry, transport measurements and extensive first-principles studies, we are able to conclusively and convincingly attribute this mid-gap state to the onset of small polarons in insulating phase VO₂ and facilitate the analysis of their kinetic behaviors with respect to temperature and structural phases. Moreover, the temperature-dependent optical studies have led to the direct observation of both conventional and correlated plasmons in the metallic and insulating phases of VO₂, respectively. The highly sensitive non-destructive photon-in photon-out approach of high-resolution spectroscopic ellipsometry and the full polarization and symmetric features of this optical experimental technique can effectively extract the underlying optical properties of VO₂ films and resolve their charge and lattice dynamics. Detailed analyses shows that the onset of small polarons may act as an intermediary to facilitate both the Peierls and Mott phase transitions in regulating the MIT processes of VO₂, as depicted in Figure 1a. The identification of a hybrid mechanism of Peierls and Mott transitions synergistically mediating the MIT processes provides a deep understanding of the actual MIT mechanism, not only for VO₂, but also for other strongly-correlated oxides, where applications in areas related to photoelectric devices are promising

II. RESULTS AND DISCUSSION

A. Validation of Sample Quality

Interfacial strain plays a pivotal role in the behavior of strongly-correlated epitaxial films grown on substrates, influencing key properties such as lattice parameters, crystal orientation, and phase stability. The lattice strain, whether tensile or compressive, arises from lattice mismatches between the film and substrate, which induces significant structural deformations in the epitaxial film. These deformations modulate electron-lattice interactions and orbital hybridization, thereby impacting the material's electronic properties. In such strongly-correlated systems, where electron-electron interactions dominate, interfacial strain can further influence the electronic correlations, modify the spin states, orbital configurations, and ultimately, control the magnetic or electronic phase transition processes.

A well-documented example of such strain effects is seen in NdNiO₃, where epitaxial strain induces local distortions of the NiO₆ octahedra, mediated by changes in oxygen stoichiometry. These distortions are crucial, as they lead to a small bandgap in the metallic system, thereby driving a metal-to-insulator transition in epitaxial NdNiO₃ thin films (41). Similarly, epitaxial strain exerts a profound influence on superconducting transition temperature (T_c) in unconventional superconductors such as in La_{2-x}Sr_xCuO₄ (LSCO). The oxygen stoichiometry, which governs the doping level and carrier concentration, is highly sensitive to the strain state of the thin film. The kinetics of oxygen exchange at the surface, influenced by both compressive and tensile strain, are crucial in determining the final oxygen content and, consequently, the superconducting properties of LSCO (42). In another example, biaxial strain in Fe₃GeTe₂ monolayers enhances ferromagnetism, with the average magnetic moment of Fe atoms increasing monotonically under tensile strain. This effect arises due to strain-induced charge redistribution and the changes in bond lengths, leading to a competition between direct exchange and super-exchange interactions that strengthens the ferromagnetic order (43).

Deciphering the physical properties governed by interfacial strain is essential for uncovering numerous potential applications and guiding future research. The development of strain engineering strategies not only facilitates the design of high-performance energy materials but also enables pioneering functional applications in strongly correlated systems, such as spintronic devices, topological quantum devices, and switchable photovoltaic and neuromorphic systems.

In the case of VO₂, interfacial strain not only shifts the MIT temperature but is also related to the formation of intermediate phases, such as the M2 and T phase, which are typically observed during the phase transition processes (44-47). These influences can be attributed to strain-induced changes in orbital occupancy, which enhance electron correlation effects. Consequently, the selection of an appropriate substrate with minimal lattice mismatch is critical for controlling the lattice strain and optimizing the phase transition characteristics of VO₂ thin films. Rutile TiO₂ emerge as an ideal substrate for VO₂ growth due to its compatible lattice parameters and thermal stability. Therefore, the VO₂ film was prepared on TiO₂ substrate by pulsed laser deposition (PLD) with atomic layer precision and the VO₂ film samples are of flat, uniform, ultra-fine morphology at the nanoscale. The thickness of the grown VO₂ layer has been measured to be ~28 nm.

X-ray diffraction (XRD) analyses and transport measurements were also conducted on the VO₂/TiO₂ films to confirm the high crystalline quality of the samples. Figure. 1b displays the XRD pattern of the 28 nm-VO₂/ TiO₂(001) sample along with the 002-plane for both the rutile TiO₂ substrate and the tetragonal-like VO₂ film at $2\theta=62.73^\circ$ and $2\theta=65.39^\circ$, respectively. The crystal quality of the film was further examined by x-ray rocking curve measurement and atomic force microscopy (AFM) (Supplementary, Section 1.3). Results from these comprehensive XRD analyses indicate the high crystalline quality of the VO₂ film where they are of similarly pristine quality as

reported in previous studies (48, 49).

Transport measurements are further conducted on the VO₂/TiO₂(001) system (Figure. 1c) where the MIT temperature and temperature-dependent resistivity of VO₂ film are once again in very good agreement with previous transport measurements involving similar VO₂ film systems (49-52). The resistivity of VO₂ film is measured to be $5.9 \times 10^{-4} \Omega \cdot \text{cm}$ in the metallic phase at 400 K. The resistivity value increases by four orders of magnitude as temperature decreases into the insulating phase. The resistivity of VO₂ film is $9.9 \Omega \cdot \text{cm}$ at 250 K. As shown in the inset of Figure. 1c, the T_{MIT} of VO₂ film during the heating cycle is 323.3 K. Meanwhile, the MIT takes place at 314.7 K during the cooling process with a small thermal hysteresis width of 8.6 K. The T_{MIT} of VO₂/TiO₂ film is lower than bulk VO₂ ($T_{\text{MIT}}=341$ K) due to the effect of in-plane tensile strain (49). As for the VO₂ sample with significantly higher oxygen vacancy concentration, it merely displays a semi-metallic behavior without any onset of the MIT (Supplemental Material, Section 1.3). The VO₂/TiO₂ sample with an abrupt transition by four orders of magnitude further affirms that our VO₂ sample meet the optical experimental requirements.

B. Temperature-dependent spectroscopic ellipsometry characterization

Spectroscopic ellipsometry represents a highly versatile tool for probing and effectively distinguishing between conventional optical band transitions and quasiparticle dynamics that arise due to many-body effects in strongly-correlated materials. It is thus widely utilized to establish the optical response and electron structures in a wide range of condensed matter systems and strongly-correlated materials at the nanoscale (53-55). Detailed optical characterization of quasiparticles was conducted on the VO₂/TiO₂ film using spectroscopic ellipsometry at temperatures between 100 K and 400 K where the MIT takes place in the photon energy range between 0.50 and 6.0 eV (Fig. 2). Results of the optical characterization using spectroscopic ellipsometry confirm our transport measurement with prominent changes to the optical parameters caused by the transition process especially with regards to its energy bands and quasiparticle dynamics in both the metallic and insulating states (12, 56). In particular, with the transport measurements confirming the MIT phenomena of the VO₂ film during the heating and cooling processes, it behaves as an insulator with a band gap (~ 0.50 eV) below 323.3 K (T_{MIT}) (12, 56). It then transforms into a metal at temperatures above 323.3 K (14). Moreover, during the spectroscopic ellipsometry characterization process, we observe the traces of three types of quasiparticles excitations, small polarons, metallic plasmons and correlated plasmons, respectively. The presence of polaron state related to small polarons is detected by analyzing the σ_1 absorption peaks in the insulating state. Next, metallic plasmons and correlated plasmons are found to distribute in the loss-function (LF) spectra. The properties of small polarons and plasmons are discussed in detail below, respectively.

The observation of polaron state

The optical conductivity of the VO₂ films (Figure 2a) were obtained from a combination of high-resolution spectroscopic ellipsometry measurements (0.5–6.0 eV) and transport measurements (0 eV). We plot the spectral weight $SW = \int_{\omega_2}^{\omega_1} \sigma_1(\omega') d\omega'$ in Figure 2b for VO₂. An enhancement of in the spectral weight of $\sigma_1(\omega)$ below 1.72 eV comes from spectral weight above 1.72 eV in metallic state. This is a contribution from the Drude response of free electrons in low-energy region (19, 57). Based on spectral-weight transfer and optical features, $\sigma_1(\omega)$ is divided into five photon energy regions: I (0-1.62 eV), II (1.62-3.28 eV), III (3.28-4.10 eV), IV (4.10-4.72 eV) and V (4.72-6.0 eV). As temperature decreases, there is an increase of spectral weight in regions II, III, IV, V and decrease of spectral weight in region I can be clearly seen in Figure 2c. The changes of the number of effective carriers per formula unit $N_{eff}(\omega)$ for different spectral regions present the same tendency with the changes of spectral weight (Supplementary, Section 2.3), as shown in Figure 2d. The changes of spectral weight and the number of the effective carriers are consistent with the conductivity behavior, indicating the occurrence of the MIT process. This is also an important sign of strong electronic correlations (58).

Figures. 3a-b display the optical conductivity, σ_1 , in the metallic ($T=400$ K) and the insulating states ($T=100$ K) elucidated from high-resolution spectroscopic ellipsometry measurements (0.5–6.0 eV). In the metallic phase at 400 K (Figure 3a), three prominent features, labelled α (~ 2.75 eV), β (~ 3.38 eV) and γ (~ 5.07 eV), can be observed. To derive a more accurate set of information on the energy position and shape of the respective features, the σ_1 spectra is then modelled using Lorentzian peaks ($L_\alpha, L_\beta, L_\gamma$) and a low-energy Drude feature based on the Drude-Lorentz model [(Figure 3a); Supplementary, Section 2.4]. The broad Drude response is a clear indication of the VO₂'s metallic properties in its metallic phase (54). Based on the analyses of the σ_1 spectra elucidated from the spectroscopic ellipsometry measurements (Supplementary, Section 2.5), the weak shoulder feature α (~ 2.75 eV) can be attributed to the optical transition from the filled O $2p$ band to the half-filled $d_{||}$ band, while the feature β (~ 3.38 eV) is ascribed to the optical transition from the filled O $2p$ band to the half-filled π^* band. Meanwhile, feature γ (~ 5.07 eV) is attributed to the optical transition between half-filled $d_{||}$ band and empty σ^* band. The positions and origins of the respective optical features and the lineshape of the σ_1 spectrum is in good agreement with previous studies (57, 59).

With the metal-to-insulator transition of VO₂ taking place at 323.3 K with the almost-simultaneous onset of Mott and Peierls transition (7, 16, 23, 60), it results in very significant changes to both the electrical conductivity and lattice structure of the VO₂ system. The Lower Hubbard band (LHB) and Upper Hubbard band (UHB) are two subbands split by half-filled Hubbard model due to the influence of Hubbard intra-atomic Coulomb repulsion energy (57). LHB is a fully-filled energy band located below the Fermi level while the UHB is an empty energy band located above the Fermi level (61). This results in a corresponding change to the σ_1 spectra below 323.3 K where VO₂

is now in the insulating phase. The insulating phase displays a sizable energy gap of ~ 0.50 eV at 100 K —in agreement with the previous report for the insulating phase of VO₂ (57). At 100 K, several distinct optical features in the σ_1 spectrum can be observed (Figure 3b). Similar to the metallic phase VO₂, σ_1 spectrum is modelled using the Lorentzian oscillators, in this case, using L_A, L_B, L_C, L_D, L_E . The feature A at ~ 1.26 eV is attributed to the optical transition between LHB (Lower Hubbard band) and π^* band. Feature C at ~ 3.39 eV in the insulating phase can be attributed to the interband transition between the LHB and UHB (Upper Hubbard band). Meanwhile, the hump feature E (~ 5.33 eV) can be accounted for by the optical transition from O $2p$ band to π^* band and from LHB to σ^* band (59).

In addition to the previously established optical absorption features as described above, two other previously unidentified features (labelled B and D) located at ~ 3.02 eV and ~ 4.26 eV, respectively, have also been observed (Figure 3b). Intriguingly, the spectral weight of features B and D are relatively low, while their energy positions do not shift with varying temperature (Supplementary, Section 3.4). Eventually, features B and D disappear above T_{MIT} along with the formation of a Drude response in the metallic phase. Based on the energy positions and the relatively small spectral weight of features B and D, it can be deduced that they are attributed to the formation of a new narrow mid-gap state (62). Thus, features B and D are optical transitions from this mid-gap state to unoccupied band.

In addition, since the low SW of σ_1 in the low photon energy region (< 2.0 eV) in the insulating state, it is difficult to accurately fit the σ_1 by using only these Lorentzian oscillators. A more in-depth analysis of the spectroscopic ellipsometry data is conducted and they are plotted in the form of a differential spectra of optical conductivity between various temperatures and 300 K in insulating state, $\Delta\sigma_1(\omega, T) = \sigma_1(\omega, T) - \sigma_1(\omega, 300 \text{ K})$, as shown in Figure 3c. An independent feature can be observed at ~ 0.7 eV (labelled Δ) across different temperatures (Supplementary, Section 2.6). This feature may be attributed to the optical transition from the mid-gap state to the π^* band. As discussed in detailed thereafter, we attribute this narrow mid-gap state to the polaron state that is present in VO₂/TiO₂ film.

The inevitable presence of oxygen vacancies (63) in VO₂ film has provided the necessary conditions in the formation of small polarons via the coupling between excess electrons and V-lattice sites. Meanwhile, in-plane tensile strain of VO₂ film increase the hopping energy of small polaron, which is beneficial for stabilizing the small polaron(32, 49). It has also been reported that the transport properties of insulating state VO₂ is dictated by the small polaron hopping dynamics, and these hopping dynamics is in turn determined by the amplitude of the thermal lattice vibrations (64, 65). Hence, we utilized the small polaron hopping model (Supplementary, Section 3.2) to model and confirm the presence of the small polarons in insulating phase VO₂. The transport curve displayed in Figure 3d shows that it is in good agreement with the theoretical

small polaron hopping model in the insulating phase below T_{MIT} (323.3 K). In the metallic state above T_{MIT} , the transport data begins to deviate from the theoretical model. This observation once again provides evidence that while small polarons are present in insulating phase VO_2 , they begin to disappear in metallic state VO_2 above T_{MIT} due to the increase in thermal lattice vibration.

Having provided the experimental evidence that small polarons are present in the insulating state VO_2 based on a detailed analysis of the transport data below and above the T_{MIT} , it is essential to clearly attribute features B and D observed in the optical spectra (Figure 3b) to the presence of the polaron state in insulating phase VO_2 . A previous theoretical study has indicated that polaron state is formed at energy region in the order of ~ 1 eV below the conduction band minimum (CBM) in large bandgap oxide systems (25). With the relatively small bandgap of insulating VO_2 , not only is the formation of the small polaron state at ~ 0.6 eV below the empty π^* band at 100 K (as discussed later in Figure 4b) theoretically consistent, but it also agrees with experimental detected polaron state in other small bandgap oxide system (66). Hence, by comparing evidences from our optical studies with previous theoretical studies detailing the presence of the polaron state in insulating phase VO_2 , they provide substantial evidences that a small polaron state is present below the Fermi level with features B (~ 3.39 eV) and D (~ 4.26 eV) in the σ_1 spectra (Figure 3b) being the optical transitions from the polaron state to the UHB and σ^* band, respectively. While our experimental studies have provided very conclusive evidences pointing to the presence of small polarons in insulating phase VO_2 , further confirmation of this quantum quasiparticle will be made via a set of computational study as discussed thereafter.

To further substantiate the experimental evidences that the mid-gap state is attributed to the formation of small polarons, detailed First-principles calculations have been performed to scrutinize the effects of electron-phonon coupling in VO_2 (Supplementary, Section 4). When excess electrons are introduced to the non-polaron VO_2 lattice (Figure 4a), these excess electrons are redistributed in the lattice where there is a tendency that they become self-trapped around vanadium sites (Figure 4b), which in turn induces the formation of the polaron state. Meanwhile, these localized electrons can also be found in neighboring vanadium sites in the vicinity where the polaron states are formed (67). In addition, the system in the non-polaron state (Figure 4a) is 0.771 eV higher in energy than the polaron state (Figure 4b). This is a clear indication that it is energetically more favorable for the excess electrons to be localized in the V lattice sites to form small polarons than in the non-polaron state where the electrons are homogeneously distributed across the lattice system. In the specific scenario where the excess charges are localized in the form displayed in Figure 4c (magnified image in Figure 4d) where small polarons are formed in the VO_2 lattice, the shape of the partial charge density implies that the excess electron mainly occupies the V $3d_{yz}$ and $3d_{xz}$ orbitals (Figure 4d). As compared to the non-polaron state counterpart, while the charge trapping at the V lattice site further increases the long V-V distance, the short V-V distance remains virtually unchanged. This is likely due to the aforementioned charge transfer from that

neighboring V site.

Further comparison is made between the visualized partial charge density of state (PDOS) of the non-polaron state as shown in Figure 4e corresponding to the homogeneous excess charge distribution of Figure 4a and the PDOS in which self-trapping of charges takes place (Figure 4f) as depicted in Figure 3b, where polaron states are formed. The PDOS of the non-polaron state VO₂ (Figure 4e) based on the GGA+U level of theory. The calculated band gap is 0.601 eV—in agreement with what is previously reported in insulating phase VO₂ (12, 56). As for the visualized PDOS where small polarons are present (Figure 4f), it is interesting to note that a mid-gap state (marked by arrow) corresponding to the polaron state can now be observed. This polaron state emerged below the Fermi level, and it mainly consists of the Vt_{2g} states. Very importantly, the results of these DFT studies show clear consistency with our experimental findings. Specifically, the mid-gap state that emerged in the visualized PDOS can be attributed to the formation of the polaron state. This provides compelling evidence to substantiate our experimental results for the presence of small polarons in insulating state VO₂.

The observation of plasmon excitations

To further analyze the quasiparticle features and opto-electronic properties of the VO₂ system and distinguish between the insulating and metallic phases, the optical loss-function (LF) is further derived with the spectra displayed in Figures 5 (Supplementary, Section 2.7). Metallic phase VO₂ shows clear metallic behavior with the prominent Drude response in σ_1 (Figure 3b) and zero-crossing of ϵ_1 (Figure 5a) at ~ 1.12 eV at 400 K. While the coincidence of the zero-crossing in the ϵ_1 spectra and the LF peak A₁ (Figure 5b) at the same photon energy position marks the presence of metallic plasmons in metallic phase VO₂. Similar observations of metallic plasmons have also been reported in previous literatures (68, 69). An essential observation is depicted in the ϵ_2 and LF spectra of VO₂ (Figures 5c-d). In the LF spectra of metallic phases (400 K) and insulating state (100 K), several features, namely B₁, B₂, B₃ and C₁, C₂, C₃, C₄, C₅ correspond one-to-one with the features in ϵ_2 spectra: B₁', B₂', B₃' and C₁', C₂', C₃', C₄', C₅', respectively. These observations suggest that the simultaneous presence of the features in both the ϵ_2 and LF spectra where they indicate a coupling between optical and plasmonic excitations in metallic and insulating VO₂ (70) (Supplementary, Section 2.8). Therefore, these corresponding features in both the metallic and insulating phases of VO₂ can be regarded as a form of correlated plasmons, arising from the collective excitations of correlated electrons. These collective features are signatures of correlated plasmonic excitation where they arise due to the presence of strong electron–electron and electron–hole interactions in the VO₂ film (71, 72).

While plasmon dynamics in the respective phases of VO₂ do not display any direct association with the system's MIT processes, the observation and characterization of

both conventional (metallic) and correlated plasmons in the distinct phases of the VO₂ film offer valuable insights into the evolution of collective charge dynamics within the system as it undergoes transformations between structural and electronic phases. Furthermore, a comprehensive grasp of plasma properties in VO₂ is crucial for their utilization in optoelectronic devices.

C. Potential mechanism relating small polarons and the MIT processes

Based on the energy positions of the major features in Figures 3a-c and combining it with previous X-ray Absorption Spectroscopic (XAS) characterization studies on the energy band and corresponding electronic structures of VO₂ (Supplementary, Section 3.4), an energy band schematic of the VO₂ system in both the metallic (400 K) and insulating phase (100 K) can be plotted as shown in Figures 6a-b, respectively (8, 16). Specifically, the polaron state emerges as a distinct feature that is located between the filled LHB and the empty π^* band in insulating phase VO₂ (Figure 6b).

Having confirmed the presence of small polarons and by analyzing the temperature-dependent energy band properties, this provides a new perspective on how small polarons facilitate the MIT processes through the opening of the bandgap in insulating VO₂ film which is yet to be fully understood. A pictorial representation of the electron dynamics above and below T_{MIT} has been provided in Figures 6c-d, respectively. Specifically, Figure 6c depicts the electron dynamics in the metallic phase at high temperature where they manifest themselves in the form of free and correlated electrons, while Figure 6d shows the localization of the electrons due to the gradual enhancement of electron-phonon interaction with decreasing temperature. In the high-temperature metallic phase where the system is significantly more energetic due to the considerable presence of thermal energy, the effects of thermal lattice vibration is significant. These high-temperature thermal effects dominate the system's lattice dynamics and along with the dynamics of the free electrons, they outweigh the effect of electron localization (Figure 6c) (73). Meanwhile, in this high-temperature metallic phase, the excitations of free and correlated electrons that manifest themselves in the form of metallic and correlated plasmons further prevent the localization of the electron due to their energetic periodic motion (Figure 6c). As a result, the collective effects of such high-temperature electron dynamics prevent the formation of small polarons. However, as temperature decreases and as it approaches T_{MIT} , there is a corresponding weakening of the thermal lattice vibrations which in turn result in the gradual enhancement of electron-phonon interaction and, at the same time, the trapping of free electrons at the V-lattice sites and in their vicinity (Figure 6d) (19, 74). This process of electron trapping due to the progressive amplification of the electron-phonon coupling greatly facilitates the formation of small polarons which is accompanied by a series of lattice distortion and symmetry breaking (30). With the increase in electron-phonon interactions, there is an amplification in lattice instability and that such structural distortions are quintessential conditions that lead to the phase transition process in the form of a Peierls transition

(23, 24, 75). Fundamentally, this phase transition process is driven by the structural instability, and in order to stabilize the once again, an energy gap opening takes place at the Fermi surface due to the formation of a charge density wave. The formation of small polarons essentially facilitates the onset of Peierls transition via the localization of charge carriers and the distortion the lattice structure, thereby driving the instability and leading to the phase transition.

At the same time, strong electron-electron interactions play a significant role in driving the metal to an insulator transition as described by the Mott theory where the competition between electron kinetic energy (charge delocalization) and Coulombic repulsion (charge localization) determines the phase of the system (76). This transition phase transition process typically takes place in systems such as transition metal oxides where electron correlations are significant (77, 78). In systems where strong electron correlations are predominant, the formation of small polarons due to electron-phonon coupling enhances the localization of charge carriers, making it easier for a system to transition to an insulating state, as required by the Mott criterion (79). In addition, the formation of small polarons can enhance the effective Coulomb repulsion between electrons. This aids in promoting the Mott insulating phase, where the electron-electron (Coulombic) repulsion dominates over kinetic energy.

In the case of VO₂ which specifically describes the dynamics of electrons in the V 3*d* channels (80), there is a significant reduction in free electrons as they become localized at the V lattice sites to form small polarons. The reduction of free electrons significantly diminishes the electronic screening effect and this reinforces the system's electron correlations especially at low temperature (19, 81). In addition, the induced localization of the electrons reduces the bandwidth of the electronic states. Consequently, the augmented electronic correlation establishes a conducive condition where it tips the balance in the competition between electron kinetic energy (charge delocalization) and Coulombic repulsion (charge localization) in favor of the insulating Mott phase.

Through the localization of electrons and the induction of lattice distortions in the formation of small polarons, the significant role that small polarons can play in mediating both the Peierls structural transition and the Mott electronic phase transition processes is evident. It can therefore be deduced that small polarons serve as an important intermediary in facilitating a hybrid mechanism comprising the aforementioned phase transitions in VO₂.

III. OUTLOOK

Currently, the cooperative Peierls-Mott model represents the most comprehensive explanation of the MIT in VO₂. Further in-depth research in the field of VO₂ is likely to benefit from advances in ultrafast spectroscopy and nanoscale imaging techniques

(10, 14). These will offer the potential to probe the MIT with unprecedented resolution. These methods could provide direct observations of the coupling between electronic and structural changes, allowing researchers to better understand the temporal sequence of events during the transition. Meanwhile, first-principles calculations and improved DMFT models are expected to offer deeper insights into the role of electronic correlations and their interaction with lattice distortions, potentially resolving long-standing ambiguities regarding the relative importance of the Peierls and Mott mechanisms (40, 82).

A promising direction for future development in this discipline involves the exploration of other diverse methods to control and tune the MIT in VO₂ via external stimuli, such as strain, doping, or electric fields. Such approaches could enable the manipulation of the transition temperature and the electronic properties of VO₂, paving the way for its integration into novel electronic and photonic devices. Applications in ultrafast switches, memory devices, and neuromorphic computing have already been proposed (9, 10, 83), and further advances in the understanding of the MIT could accelerate the realization of these technologies. The ability to modulate the MIT through precise control of external parameters represents a crucial step toward harnessing the unique properties of VO₂ for practical applications, while also offering a rich platform for exploring the fundamental physics of correlated electron systems.

Beyond the domain of the VO₂ system and the mechanisms underlying the MIT process, the development of polaron research presents new prospects and opportunities where they encompass a diverse variety of materials and phenomena. Polarons play a crucial role in determining properties such as electrical conductivity, surface reactivity, and magnetoresistance in various materials, including transition-metal oxides, conducting polymers, and 2D materials (25). Computational tools such as density functional theory (DFT) and dynamical mean-field theory (DMFT) have enabled more precise calculations of polaron properties, such as binding energy, effective mass, and mobility. Despite these advances, theoretical models like Landau-Pekar and Fröhlich's pose considerable limits in describing real materials in an effective way. This is because many theoretical models oversimplify the electron-phonon interactions and are unable to account for the dynamics in non-polar systems (84, 85). Current challenges include the need for models that capture both short- and long-range coupling and the accurate representation of polaron behavior in hybrid materials like halide perovskites, where complex electron-phonon interactions complicate the picture.

Looking ahead, advancing polaron research will require more sophisticated models and computational techniques that can better integrate first-principles calculations with realistic material properties. One key area of focus will be the development of unified frameworks that address both short-range and long-range electron-phonon interactions. Additionally, research into low-dimensional systems, such as 2D materials, is expected to yield new and intriguing insights into how polarons behave under spatial confinement. Polaron studies will also expand into multi-polaron systems, where

interactions between multiple polarons may lead to novel phenomena such as bipolaron formation, with implications for high-temperature superconductivity. The role of polarons at material interfaces, especially in van der Waals heterostructures, will be another area of intense study, potentially opening new paths for electronic and optoelectronic devices.

Polaronic effects hold promise for a wide range of applications. In thermoelectric materials, controlling polaron mobility could enhance energy efficiency, while in organic semiconductors, understanding polaron dynamics is crucial for optimizing charge transport. Hybrid perovskite solar cells, where polarons influence both light absorption and charge separation, represent another key application area. In catalysis, the role of polarons in mediating surface reactions could be harnessed to improve catalytic performance. Beyond these practical applications, polarons are also relevant in emerging quantum technologies, where they could be used to manipulate charge and spin states in quantum dots and other nanoscale devices. This potential for applications in quantum computing and memory devices makes polaron research a vital field for future technological advancements.

IV. CONCLUSION

In conclusion, we have clearly and convincingly demonstrated the presence of small polarons in insulating phase VO₂ film through a comprehensive study that combines a range of experimental and first-principles investigation. This study highlights the small polarons intimately related phase transition processes underscore the assertion that both electron-phonon and electron-electron interactions may play crucial roles in driving the metal-insulator transition processes in VO₂ as well as in other strongly-correlated systems. Further experimental observations have also shown the presence of conventional and correlated plasmons in VO₂ system. Meanwhile, these new insights in strongly-correlated oxides allow for potential applications related to energy conversion, such as thermoelectric generators, neuromorphic sensors and photoelectric devices. Hence, regulating quasiparticles generation and dynamics is undoubtedly advantageous to further device applications.

SUPPLEMENTARY MATERIAL

Discussion on sample preparation (PLD method); crystalline quality characterizations (XRD, X-ray rocking curve, transport measurements); Spectroscopic Ellipsometry measurements (principle, methods, model, and data analysis); detection of quasiparticles (analysis of small polarons, metallic plasmons, and correlated plasmons; illustration of electrical band structure and theoretical model fitting); details of first-principles calculations; supplementary figures and associated references (PDF).

AUTHOR CONTRIBUTIONS

X.L., T.Y., S.C. contributed equally to this work. X.Y. conceived the project. K.H., S.Z., T.V., S.C. synthesized the samples and K.H., S.Z. performed the electron transport experiments and analyzed the data, C.S.T. performed the XRD experiments and analyzed the data and X.L., C.S.T., M.S., M.C., S.S.L. performed the SE experiments and analyzed the data. T.Y., M.Y. performed the DFT calculations. X.L. and C.S.T. wrote the manuscript, with input from all the authors.

Conflict of Interest

The authors have no conflicts to disclose.

ACKNOWLEDGMENTS

This work was supported by National Natural Science Foundation of China (Grant No. 52172271, 12374378, 52307026), the National Key R&D Program of China (Grant No. 2022YFE03150200), Shanghai Science and Technology Innovation Program (Grant No. 22511100200, 23511101600), the Strategic Priority Research Program of the Chinese Academy of Sciences (Grant No. XDB25000000). J.W. acknowledges the Advanced Manufacturing and Engineering Young Individual Research Grant (AME YIRG Grant No. A2084c0170) and the SERC Central Research Fund (CRF). C.S.T acknowledges the support from the NUS Emerging Scientist Fellowship. S.S.L. would like to thank the funding support from National Natural Science Foundation of China (NSFC) (No. 62175206). M.Y. acknowledges the funding support from The Hong Kong Polytechnic University (project number: 1-BE47, ZE0C, ZE2F and ZE2X).

DATA AVAILABILITY

The data that support the findings of this study are available within the article and its supplementary material.

Reference

1. I. F. Herbut, Effective theory of high-temperature superconductors. *Phys Rev Lett* **94**, 237001 (2005).
2. J. Mannhart *et al.*, Generation of Magnetic Flux by Single Grain Boundaries of YBa₂Cu₃O_{7-x}. *Phys Rev Lett* **77**, 2782 (1996).
3. L. Nie *et al.*, Charge-density-wave-driven electronic nematicity in a kagome superconductor. *Nature* **604**, 59-64 (2022).
4. S. Han *et al.*, Orbital-Hybridization-Driven Charge Density Wave Transition in CsV₃Sb₅ Kagome Superconductor. *Adv Mater* **35**, 2209010 (2022).
5. H. Zhao *et al.*, Smectic pair-density-wave order in EuRbFe₄As₄. *Nature* **618**, 940-945 (2023).
6. Q. Gu *et al.*, Detection of a pair density wave state in UTe₂. *Nature* **618**, 921-927 (2023).
7. S. Biermann, A. Poteryaev, A. I. Lichtenstein, A. Georges, Dynamical singlets and correlation-assisted Peierls transition in VO₂. *Phys Rev Lett* **94**, 026404 (2005).
8. N. B. Aetukuri *et al.*, Control of the metal–insulator transition in vanadium dioxide by modifying orbital occupancy. *Nat. Phys* **9**, 661-666 (2013).
9. G. Li *et al.*, Photo-induced non-volatile VO₂ phase transition for neuromorphic ultraviolet sensors. *Nat Commun* **13**, 1729 (2022).
10. A. S. Johnson *et al.*, Ultrafast X-ray imaging of the light-induced phase transition in VO₂. *Nat. Phys* **19**, 215-220 (2022).
11. M. Li, S. Magdassi, Y. Gao, Y. Long, Hydrothermal Synthesis of VO₂ Polymorphs: Advantages, Challenges and Prospects for the Application of Energy Efficient Smart Windows. *Small* **13**, 1701147 (2017).
12. S. Cheng *et al.*, Inherent stochasticity during insulator-metal transition in VO₂. *PNAS* **118**, 2105895118 (2021).
13. C. Wu, F. Feng, Y. Xie, Design of vanadium oxide structures with controllable electrical properties for energy applications. *Chem Soc Rev* **42**, 5157-5183 (2013).
14. C. Xu *et al.*, Transient dynamics of the phase transition in VO₂ revealed by mega-electron-volt ultrafast electron diffraction. *Nat Commun* **14**, 1265 (2023).
15. A. Cavalleri, T. Dekorsy, H. H. W. Chong, J. C. Kieffer, R. W. Schoenlein, Evidence for a structurally-driven insulator-to-metal transition in VO₂: A view from the ultrafast timescale. *Phys. Rev. B* **70**, 161102 (2004).
16. T. C. Koethe *et al.*, Transfer of spectral weight and symmetry across the metal-insulator transition in VO₂. *Phys Rev Lett* **97**, 116402 (2006).
17. V. Jonsson *et al.*, Photoelectron dispersion in metallic and insulating VO₂ thin films. *Physical Review Research* **3**, 033286 (2021).
18. S. Kittiwatanakul, S. A. Wolf, J. Lu, Large epitaxial bi-axial strain induces a Mott-like phase transition in VO₂. *Applied Physics Letters* **105** (2014).
19. K. Okazaki, S. Sugai, Y. Muraoka, Z. Hiroi, Role of electron-electron and electron-phonon interaction effects in the optical conductivity of VO₂. *Phys. Rev. B* **73**, 165116 (2006).
20. A. Garg, M. Randeria, N. Trivedi, Strong correlations make high-temperature superconductors robust against disorder. *Nature Physics* **4**, 762-765 (2008).
21. J. Z. R. G. Moore, V. B. Nascimento, R. Jin, Jiandong Guo, G.T. Wang, Z. Fang, D. Mandrus, and E. W. Plummer, A Surface-Tailored, Purely Electronic, Mott Metal-to-Insulator Transition.

- Science* **318**, 615-619 (2007).
22. W. H. Brito, M. C. Aguiar, K. Haule, G. Kotliar, Metal-Insulator Transition in VO₂: A DFT+DMFT Perspective. *Phys Rev Lett* **117**, 056402 (2016).
 23. T. Yao *et al.*, Understanding the nature of the kinetic process in a VO₂ metal-insulator transition. *Phys Rev Lett* **105**, 226405 (2010).
 24. F. Grandi, A. Amaricci, M. Fabrizio, Unraveling the Mott-Peierls intrigue in vanadium dioxide. *Physical Review Research* **2**, 013298 (2020).
 25. C. Franchini, M. Reticcioli, M. Setvin, U. Diebold, Polarons in materials. *Nat Rev Mater* **6**, 560-586 (2021).
 26. S. A. Maier, S. R. Andrews, L. Martin-Moreno, F. J. Garcia-Vidal, Terahertz surface plasmon-polariton propagation and focusing on periodically corrugated metal wires. *Phys Rev Lett* **97**, 176805 (2006).
 27. L. D. Landau, Über die bewegung der elektronen im kristallgitter. *Phys. Z. Sowjetunion* **3**, 664–645 (1933).
 28. S. I. PEKAR, Local Quantum States of Electrons in an Ideal Ion Crystal. *Zh. Eksp. Teor. Fiz.* **16**, 341–348 (1946).
 29. M. Reticcioli, U. Diebold, G. Kresse, C. Franchini, *Small Polarons in Transition Metal Oxides*, Small Polarons in Transition Metal Oxides (Reticcioli, M., Diebold, U., Kresse, G., Franchini, C. (2020). Small Polarons in Transition Metal Oxides. In: Andreoni, W., Yip, S. (eds) Handbook of Materials Modeling. Springer, Cham., 2020), 10.1007/978-3-319-44680-6_52 https://doi.org/10.1007/978-3-319-44680-6_52, pp. 1035-1073.
 30. C. Franchini, G. Kresse, R. Podloucky, Polaronic hole trapping in doped BaBiO₃. *Phys Rev Lett* **102**, 256402 (2009).
 31. D. V. Averyanov *et al.*, Fine structure of metal–insulator transition in EuO resolved by doping engineering. *Nanotechnology* **29**, 195706 (2018).
 32. C. S. Tang *et al.*, Detection of two-dimensional small polarons at oxide interfaces by optical spectroscopy. *Applied Physics Reviews* **10**, 031406 (2023).
 33. S. Zhang *et al.*, Enhanced Superconducting State in FeSe/SrTiO₃ by a Dynamic Interfacial Polaron Mechanism. *Phys Rev Lett* **122**, 066802 (2019).
 34. T. Nishio, J. Ahmad, H. Uwe, Spectroscopic Observation of Bipolaronic Point Defects in Ba_{1-x}K_xBiO₃. *Physical Review Letters* **95**, 176403 (2005).
 35. C. Cancellieri *et al.*, Polaronic metal state at the LaAlO₃/SrTiO₃ interface. *Nat Commun* **7**, 10386 (2016).
 36. P. Suo *et al.*, Observation of Negative Terahertz Photoconductivity in Large Area Type-II Dirac Semimetal PtTe₂. *Physical Review Letters* **126**, 227402 (2021).
 37. N. Kumar, A. Rua, J. Lu, F. Fernandez, S. Lysenko, Ultrafast Excited-State Dynamics of V₃O₅ as a Signature of a Photoinduced Insulator-Metal Phase Transition. *Phys Rev Lett* **119**, 057602 (2017).
 38. N. F. Mott, Metal-Insulator Transition. *Rev. Mod. Phys.* **40**, 677-683 (1968).
 39. J. B. Goodenough, The Two Components of the Crystallographic Transition in VO₂*. *J Solid State Chem* **3**, 490-500 (1971).
 40. J. Kaur, M. L. H. Chandrappa, C. Chen, S. P. Ong, Polaron-induced metal-to-insulator transition in vanadium oxides from density functional theory calculations. *Physical Review B* **107**, 125162 (2023).

41. T. H. Kim *et al.*, Strain-driven disproportionation at a correlated oxide metal-insulator transition. *Physical Review B* **101**, 121105(R) (2020).
42. T. L. Meyer *et al.*, Strain control of oxygen kinetics in the Ruddlesden-Popper oxide La(1.85)Sr(0.15)CuO(4). *Nat Commun* **9**, 92 (2018).
43. X. Hu *et al.*, Enhanced Ferromagnetism and Tunable Magnetism in Fe(3)GeTe(2) Monolayer by Strain Engineering. *ACS Appl Mater Interfaces* **12**, 26367-26373 (2020).
44. E. Abreu *et al.*, THz spectroscopy of VO₂ epitaxial films: controlling the anisotropic properties through strain engineering. *New Journal of Physics* **14**, 083026 (2012).
45. H. Guo *et al.*, Mechanics and dynamics of the strain-induced M1-M2 structural phase transition in individual VO(2) nanowires. *Nano Lett* **11**, 3207-3213 (2011).
46. A. Tselev *et al.*, Symmetry relationship and strain-induced transitions between insulating M1 and M2 and metallic R phases of vanadium dioxide. *Nano Lett* **10**, 4409-4416 (2010).
47. J. H. Park *et al.*, Measurement of a solid-state triple point at the metal-insulator transition in VO₂. *Nature* **500**, 431-434 (2013).
48. C. N. Mihailescu *et al.*, Ambiguous Role of Growth-Induced Defects on the Semiconductor-to-Metal Characteristics in Epitaxial VO₂/TiO₂ Thin Films. *ACS Appl Mater Interfaces* **10**, 14132-14144 (2018).
49. Y. Muraoka, Z. Hiroi, Metal-insulator transition of VO₂ thin films grown on TiO₂ (001) and (110) substrates. *Appl. Phys. Lett* **80**, 583-585 (2002).
50. N. A. Jaewoo Jeong, Tanja Graf, Thomas D. Schladt, Mahesh G. Samant, Stuart S. P. Parkin, Suppression of Metal-Insulator Transition in VO₂ by Electric Field-Induced Oxygen Vacancy Formation. *Science* **339**, 1402-1405 (2013).
51. J. Lee. *et al.*, Isostructural metal-insulator transition in VO₂. *Science* **362**, 1037-1040 (2018).
52. H. Paik *et al.*, Transport properties of ultra-thin VO₂ films on (001) TiO₂ grown by reactive molecular-beam epitaxy. *Appl. Phys. Lett* **107**, 163101 (2015).
53. X. Yin *et al.*, Unraveling how electronic and spin structures control macroscopic properties of manganite ultra-thin films. *NPG Asia Materials* **7**, e196-e196 (2015).
54. Z. Q. Li *et al.*, Dirac charge dynamics in graphene by infrared spectroscopy. *Nat. Phys* **4**, 532-535 (2008).
55. A. T. S. Wee, X. Yin, C. S. Tang, *Introduction to Spectroscopic Ellipsometry of Thin Film Materials: Instrumentation, Data Analysis, and Applications* (Wiley-VCH, Weinheim, 2022), pp. 187.
56. J. Wei, Z. Wang, W. Chen, D. H. Cobden, New aspects of the metal-insulator transition in single-domain vanadium dioxide nanobeams. *Nat Nanotechnol* **4**, 420-424 (2009).
57. M. M. Qazilbash *et al.*, Electrodynamics of the vanadium oxides VO₂ and V₂O₃. *Phys. Rev. B* **77**, 115121 (2008).
58. X. Yin *et al.*, Modulation of Manganite Nanofilm Properties Mediated by Strong Influence of Strontium Titanate Excitons. *ACS Applied Materials & Interfaces* **10**, 35563-35570 (2017).
59. W. W. Li, Q. Yu, J. R. Liang, Intrinsic evolutions of optical functions, band gap, and higher-energy electronic transitions in VO₂ film near the metal-insulator transition region. *Appl. Phys. Lett* **99**, 241903 (2011).
60. M. W. Haverkort *et al.*, Orbital-assisted metal-insulator transition in VO₂. *Phys Rev Lett* **95**, 196404 (2005).
61. M. Nazari *et al.*, Temperature dependence of the optical properties of VO₂ deposited on sapphire

- with different orientations. *Physical Review B* **87**, 035142 (2013).
62. N. Nagatsuka, K. Kato, M. Wilde, K. Fukutani, Absence of midgap states due to excess electrons donated by adsorbed hydrogen on the anatase TiO₂(101) surface. *Phys. Rev. B* **105**, 045424 (2022).
 63. W.-J. Yin, B. Wen, C. Zhou, A. Selloni, L.-M. Liu, Excess electrons in reduced rutile and anatase TiO₂. *Surf. Sci. Rep* **73**, 58-82 (2018).
 64. X. Zhong, P. LeClair, S. K. Sarker, A. Gupta, Metal-insulator transition in epitaxial VO₂ thin films on TiO₂(100). *Phys. Rev. B* **86**, 094114 (2012).
 65. V. N. Andreev, V. A. Klimov, Electrical conductivity of the semiconducting phase in vanadium dioxide single crystals. *Phys. Solid State* **49**, 2251-2255 (2007).
 66. T. J. Smart, T. A. Pham, Y. Ping, T. Ogitsu, Optical absorption induced by small polaron formation in transition metal oxides: The case of Co₃O₄. *Phys. Rev. Mater* **3**, 102401(R) (2019).
 67. K. Martens *et al.*, Field Effect and Strongly Localized Carriers in the Metal-Insulator Transition Material VO₂. *Phys Rev Lett* **115**, 196401 (2015).
 68. N. Nucker *et al.*, Plasmons and interband transitions in Bi₂Sr₂CaCu₂O₈. *Phys Rev B Condens Matter* **39**, 12379-12382 (1989).
 69. A. Bianconi, S. Stizza, R. Bernardini, Critical behavior of the plasmon resonance at the metal-insulator transition in VO₂. *Phys. Rev. B* **24**, 4406-4411 (1981).
 70. T. C. Asmara *et al.*, Tunable and low-loss correlated plasmons in Mott-like insulating oxides. *Nat Commun* **8**, 15271 (2017).
 71. X. Yin *et al.*, Quantum Correlated Plasmons and Their Tunability in Undoped and Doped Mott-Insulator Cuprates. *ACS Photonics* **6**, 3281-3289 (2019).
 72. E. G. van Loon, H. Hafermann, A. I. Lichtenstein, A. N. Rubtsov, M. I. Katsnelson, Plasmons in strongly correlated systems: spectral weight transfer and renormalized dispersion. *Phys Rev Lett* **113**, 246407 (2014).
 73. I. H. Hwang, Z. Jin, C. I. Park, S. W. Han, The influence of structural disorder and phonon on metal-to-insulator transition of VO₂. *Sci Rep* **7**, 14802 (2017).
 74. K.-X. Xu *et al.*, High-order Raman scattering mediated by self-trapped exciton in halide double perovskite. *Phys. Rev. B* **106**, 085205 (2022).
 75. Y. Liang, X. Yuan, Y. Gao, W. Zhang, P. Zhang, Phonon-assisted crossover from a nonmagnetic Peierls insulator to a magnetic Stoner metal. *Phys Rev Lett* **113**, 176401 (2014).
 76. M. M. Qazilbash *et al.*, Mott transition in VO₂ revealed by infrared spectroscopy and nano-imaging. *Science* **318**, 1750-1753 (2007).
 77. Y. Xu *et al.*, Interaction-Driven Metal-Insulator Transition with Charge Fractionalization. *Physical Review X* **12** (2022).
 78. B. H. Moon, Metal-insulator transition in two-dimensional transition metal dichalcogenides. *Emergent Materials* **4**, 989-998 (2021).
 79. A. Pergament, Metal-insulator transition: the Mott criterion and coherence length. *Journal of Physics: Condensed Matter* **15**, 3217-3223 (2003).
 80. L. H. Yeo *et al.*, Anomalous spectral-weight transfers unraveling oxygen screening and electronic correlations in the insulator-metal transition of VO₂. *Phys. Rev. B* **91**, 081112(R) (2015).
 81. A. Zylbersztein, N. F. Mott, Metal-insulator transition in vanadium dioxide. *Phys. Rev. B* **11**, 4383-4395 (1975).

82. P. Mlkvik, M. E. Merkel, N. A. Spaldin, C. Ederer, Single-site DFT+DMFT for vanadium dioxide using bond-centered orbitals. *Physical Review Research* **6**, 033122 ((2024).
83. F. H. Chen *et al.*, Control of the metal-insulator transition in VO₂ epitaxial film by modifying carrier density. *ACS Appl Mater Interfaces* **7**, 6875-6881 (2015).
84. A. S. Alexandrov, J. T. Devreese, *Advances in Polaron Physics* (Springer-Verlag Berlin Heidelberg 2010).
85. W. H. Sio, C. Verdi, S. Ponc e, F. Giustino, Ab initio theory of polarons: Formalism and applications. *Physical Review B* **99**, 235139 (2019).

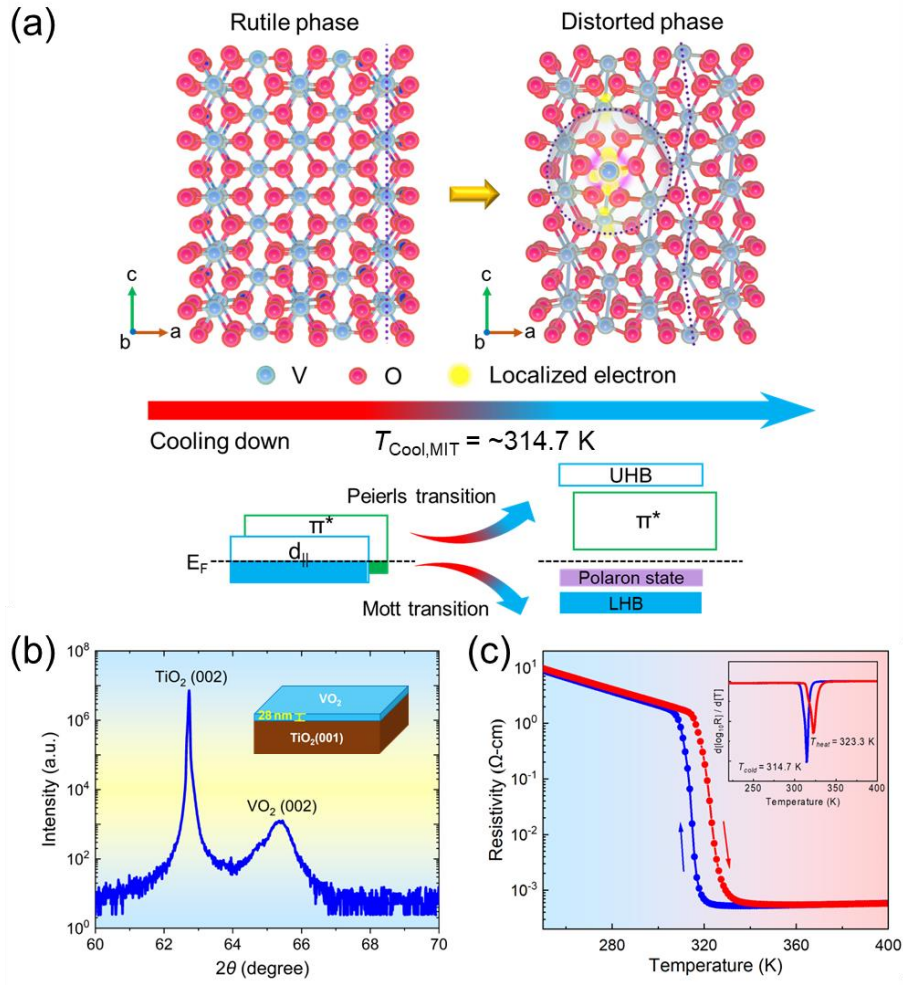


Figure 1. The intermediary role that small polarons play in the MIT processes of VO_2/TiO_2 film and results from the XRD and transport measurement on the sample. (a) Schematic that depicts the localized electrons in the vicinity of a distorted VO_2 lattice which is indicative that small polarons are present in insulating phase VO_2 . Presence of small polarons may possibly mediate the onset of Peierls and Mott phase transitions near $T_{cool, MIT}$ (314.7 K) during the cooling processes. These physical terms E_F (Fermi level), π^* , $d_{||}$, UHB (Upper Hubbard Band) and LHB (Lower Hubbard Band) present different band structure of VO_2 system. Peierls transition and Mott transition are two types involving MIT processes. (b) Structural analysis of epitaxial VO_2 film grown on $TiO_2(001)$ substrate based on XRD characterization. θ - 2θ scan around the $TiO_2(002)$ and $VO_2(002)$ peak where no other peaks have been found. (c) Temperature-dependent resistivity curves of VO_2 films grown on $TiO_2(001)$ substrate. The inset shows the corresponding $d[\log_{10}(R)]/dT$ curves.

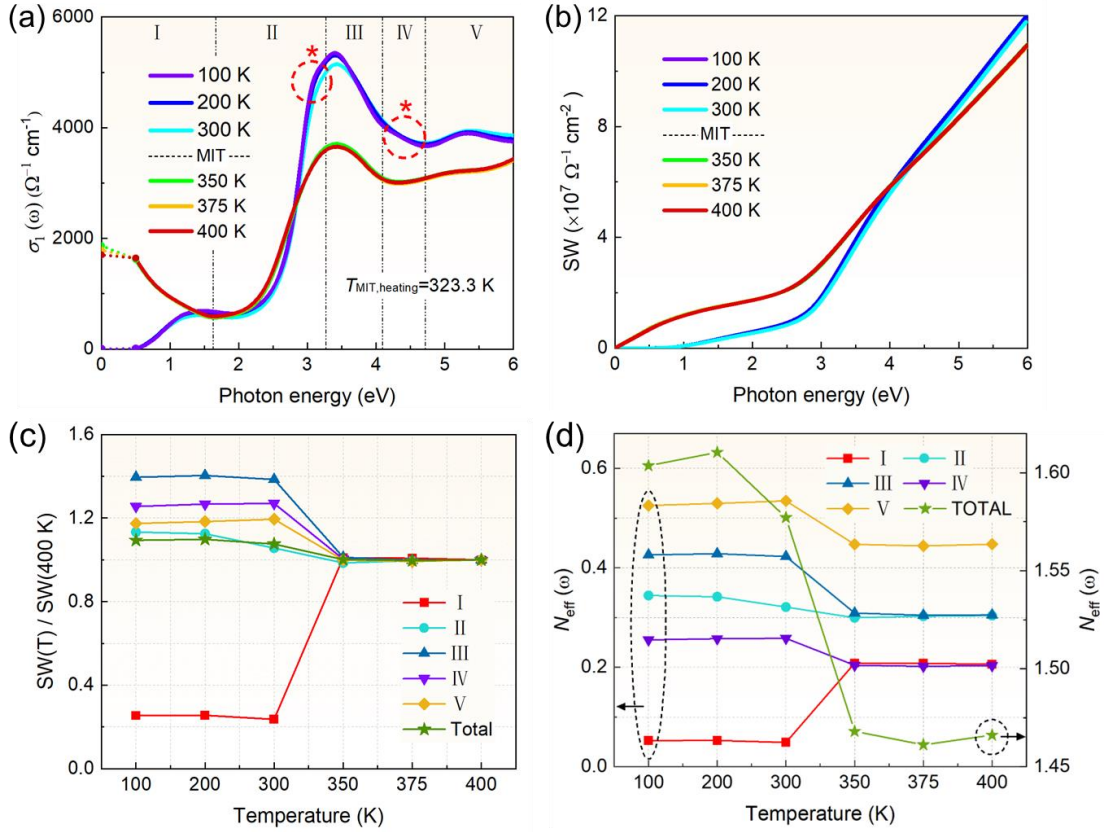


Figure 2. Optical conductivity, σ_1 , spectra of the VO₂/TiO₂ film. (a) σ_1 spectra of VO₂/TiO₂(001) film from 0 to 6.0 eV at the respective temperatures in both its insulating and metallic phases (where $T_{\text{MIT}} = \sim 323.3 \text{ K}$). The $\sigma_1(0)$ is obtained from transport measurements and the linear interpolation is used to estimate the σ_1 from 0 to 0.50 eV. (b) The spectral weight SW is plotted by integrating the $\sigma_1(\omega)$. (c) Ratio of the spectral weight defined as $\text{SW}(T)/\text{SW}(400 \text{ K})$ and (d) The number of the effective carriers per formula unit [$N_{\text{eff}}(\omega)$] as a function of temperature in different spectral regions: I (0-1.62 eV), II (1.62-3.28 eV), III (3.28-4.10 eV), IV (4.10-4.72 eV), V (4.72-6.0 eV) and total (0-6.0 eV). Temperature is described as T (K).

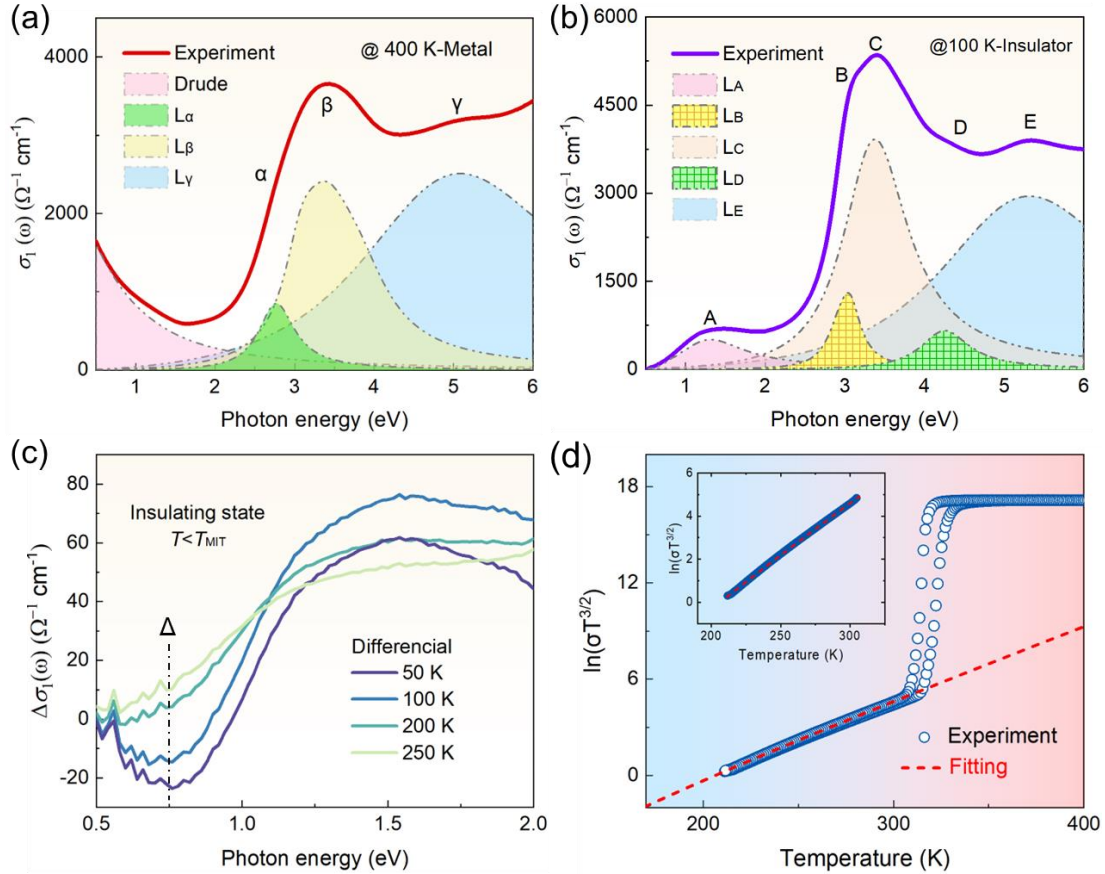


Figure 3. Optical feature fitting and transport measurements of the VO₂/TiO₂ film. (a-b) σ_1 spectra of VO₂ and their respective fitting curves in (a) metallic phase VO₂ film at 400 K, and (b) insulating phase VO₂ film at 100 K to account for the respective peak features present in the spectra. The solid curve represents the actual σ_1 spectra while the peaks in their respective colors represent the fitted curves. A Drude feature has been added to metallic phase VO₂. (c) The differential spectra of the optical conductivity $\Delta\sigma_1(\omega, T) = \sigma_1(\omega, T) - \sigma_1(\omega, 300 \text{ K})$ for VO₂/TiO₂ film. The symbol ‘ Δ ’ ($\sim 0.7 \text{ eV}$) denotes an optical feature detected in the $\Delta\sigma_1(\omega, T)$ spectrum. (d) $\ln(\sigma T^{3/2})$ vs T curves. The red dash line is fitted to the experimental data using the hopping conductivity of small polarons. Inset: $\ln(\sigma T^{3/2})$ vs T below T_{MIT} . Indicating that the activated behavior of small polarons only takes place in the insulating phase below T_{MIT} . Data shows very good agreement with the theoretical fitting line.

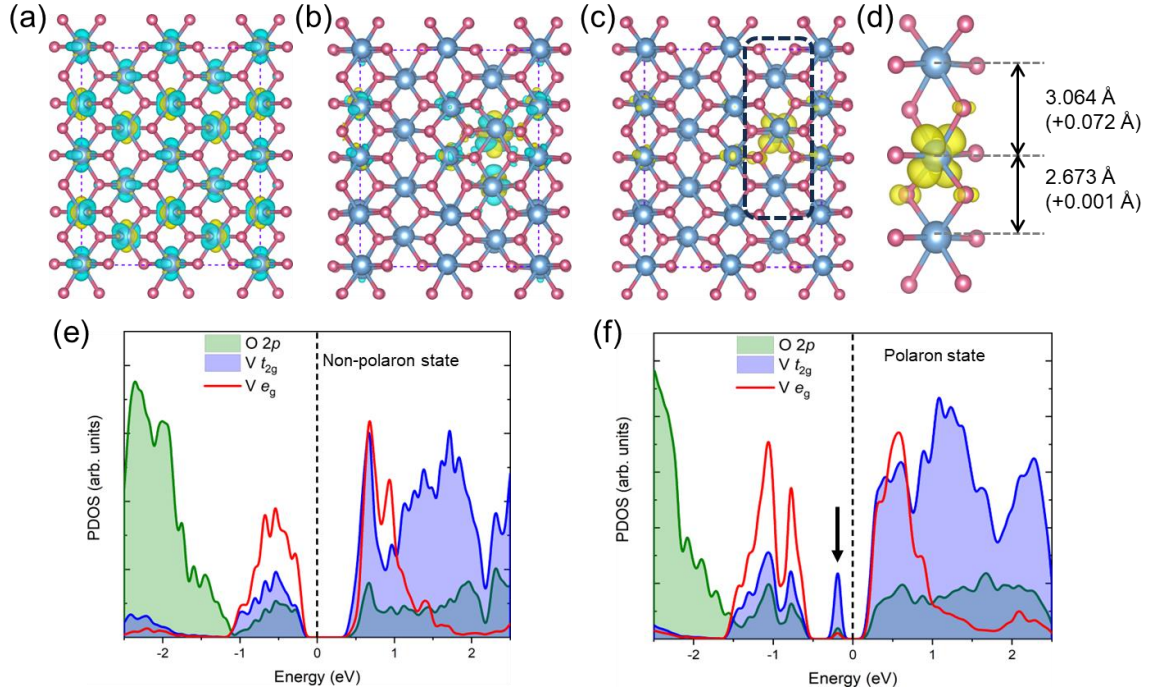


Figure 4. First-principles calculations and plasmon excitation spectra of the VO₂/TiO₂ film. Excess charge density distribution in the (a) non-polaron state and (b) polaron state. The charge accumulation/depletion is denoted by the yellow/cyan iso-surfaces with an iso-value of 0.0015 e/Å³ (non-polaron state) and 0.007 e/Å³ (polaron state), respectively. (c) Visualized partial charge density associated with the mid-gap state described thereafter in (f). (d) Magnification of the localized charges enclosed in the black dashed rectangle of (c) with the iso-value is set to 0.007 e/Å³. (e) Projected density of states (PDOS) of non-polaron VO₂ and (f) PDOS of VO₂ in the polaron state where the Fermi level has been set to 0 in both scenarios.

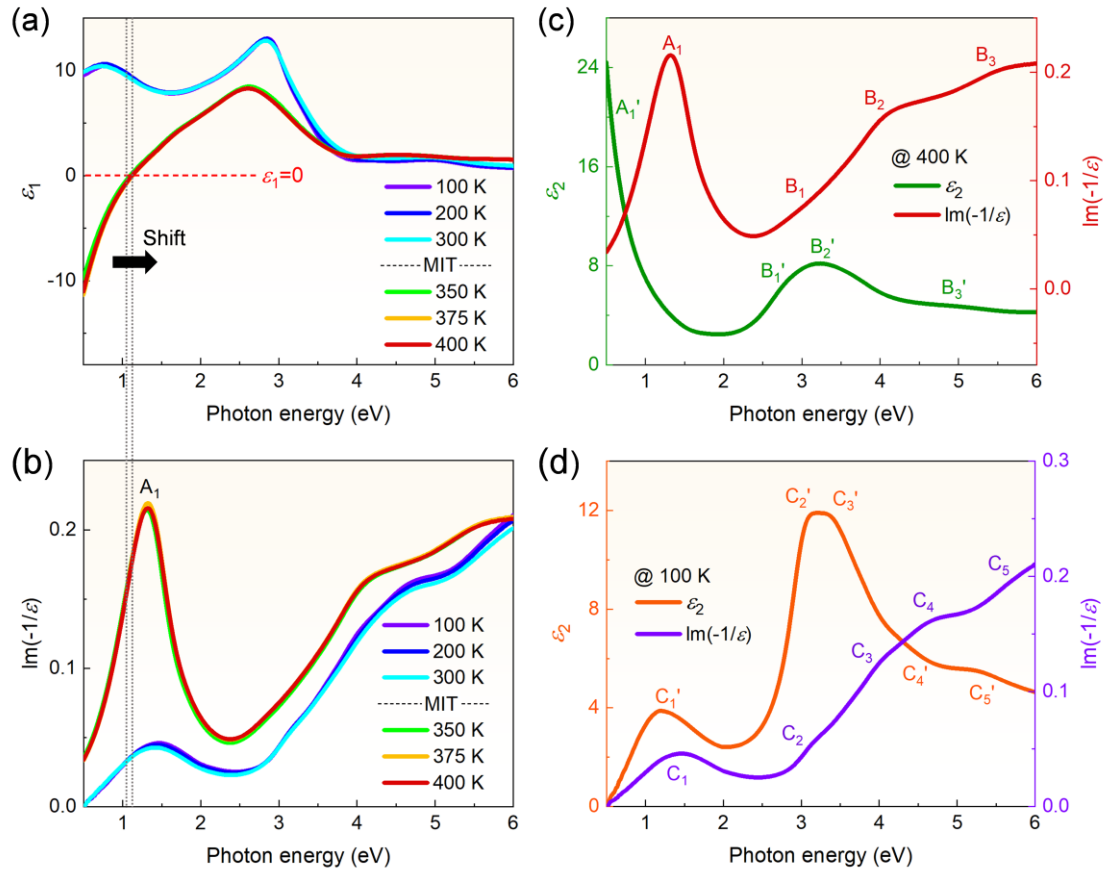


Figure 5. The observation of plasmon excitations. (a) Real component of the dielectric function, ϵ_1 , at the respective temperatures above and below T_{MIT} and, (b) shows the corresponding Loss Function (LF) spectra. (c-d) The ϵ_2 and LF spectra of VO₂ film at (c) 400 K and (d) 100 K.

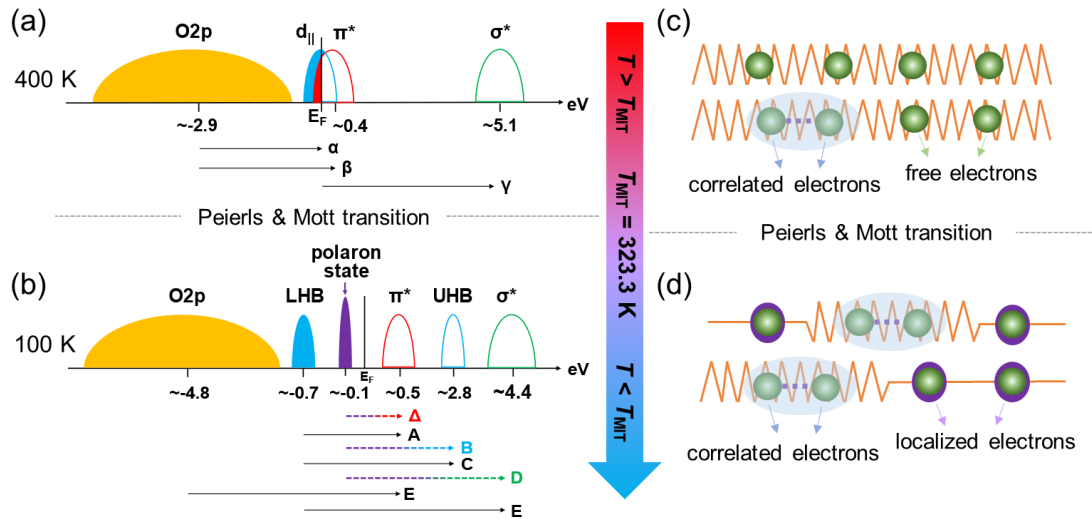


Figure 6. Changes to the electronic structures of the VO_2/TiO_2 film during the MIT process. Schematic models of the electron structures for VO_2 in (a) the metallic state at 400 K, and (b) in the insulating state at 100 K. The arrows and the respective letters denote the interband transitions in metallic and insulating phase VO_2 as registered by the optical measurements previously displayed in Figures 3a-b, respectively. (c-d) Schematics depicting how electron correlations evolve during the MIT transition process. (c) Electrons are delocalized in the metallic state where collective oscillations of free electrons and correlated electrons are present. (d) As the temperature decreases, the number of correlated electrons increases as an increasing number of electrons are localized. This results in the presence and coexistence of correlated electrons and small polarons in insulating phase VO_2 .

Supplemental Information

Small polarons mediated near-room-temperature metal-insulator transition in vanadium dioxide and their hopping dynamics

Xiongfang Liu^{1,#}, Tong Yang^{2,#}, Shanquan Chen^{3,#}, Jing Wu⁴, Chi Sin Tang^{1,5,}, Yuanjie Ning¹, Zuhuang Chen³, Liang Dai¹, Mengxia Sun¹, Mingyao Chen¹, Kun Han⁶, Difan Zhou¹, Shengwei Zeng⁴, Shuo Sun¹, Sensen Li⁷, Ming Yang^{2,*}, Mark B. H. Breese^{5,8}, Chuanbing Cai¹, Thirumalai Venkatesan⁹, Andrew T. S. Wee^{8,10}, Xinmao Yin^{1,*}*

¹Shanghai Key Laboratory of High Temperature Superconductors, Institute for Quantum Science and Technology, Department of Physics, Shanghai University, Shanghai 200444, China

²Department of Applied Physics, The Hong Kong Polytechnic University, Kowloon, Hong Kong, 100872, China

³School of Materials Science and Engineering Harbin Institute of Technology, Shenzhen 518055, China

⁴Institute of Materials Research and Engineering (IMRE), Agency for Science, Technology and Research (A*STAR), 2 Fusionopolis Way, Innovis #08-03, Singapore 138634, Singapore

⁵Singapore Synchrotron Light Source (SSLS), National University of Singapore, Singapore 117603, Singapore

⁶Information Materials and Intelligent Sensing Laboratory of Anhui Province, Institutes of Physical Science and Information Technology, Anhui University, Hefei 230601, China

⁷Department of Electronic Engineering, School of Electronic Science and Engineering, Xiamen University, Xiamen 361005, China

⁸Department of Physics, Faculty of Science, National University of Singapore, Singapore 117542, Singapore

⁹Center for Quantum Research and Technology, University of Oklahoma, Norman, Oklahoma 73019, USA

¹⁰Centre for Advanced 2D Materials and Graphene Research, National University of Singapore, Singapore 117546, Singapore

#These authors contributed equally to this work.

*Corresponding author: slscst@nus.edu.sg (C.S.T.); kevin.m.yang@polyu.edu.hk (M.Y.); yinxinmao@shu.edu.cn (X.Y.)

Content

1. Crystal Structure of Mott Insulator VO₂
 - 1.1. Crystallographic Configuration of VO₂
 - 1.2. Sample Preparation
 - 1.3. Crystalline Quality Characterization of VO₂ (High-resolution X-ray Diffraction, Electron Transport Measurements and Atomic Force Microscopy)
 2. Temperature-dependent Spectroscopic Ellipsometry Measurements
 - 2.1. Experimental Principle and Methods
 - 2.2. Temperature-dependent Spectroscopic Ellipsometry Characterization
 - 2.3. The number of Effective Carriers
 - 2.4. Drude-Lorentz Model
 - 2.5. Optical Transitions Analysis in Optical Conductivity Spectra
 - 2.6. Plotting the Differential Spectra of the Optical Conductivity
 - 2.7. Dynamical Response Loss-Function
 - 2.8. The Observation of Plasmon Excitations
 3. Small Polarons Analysis
 - 3.1. The Characteristics of Small Polarons
 - 3.2. Small Polaron Hopping Model
 - 3.3. Small Polaron State
 - 3.4. Analysis for The Band Structures
 4. First-principles Calculations
- References

1. Crystal Structure of Mott Insulator VO₂

1.1. Crystallographic Configuration of VO₂

VO₂ is a Mott insulator with reversible structural transition properties¹. Close to the metal-insulator transition temperature (T_{MIT}) at or near room temperature, electronic phase transitions (the electrical resistance changes by several orders of magnitude between the metallic and insulating phases²) and structural transition (the dimerization of V⁴⁺ ions along the C_R axis direction, system from rutile phase to monoclinic phase³) occur almost simultaneously.

In the metallic phase above T_{MIT} , VO₂ has a rutile structure⁴ (Figure. S1a). The neighboring V–V bond is ~ 2.85 Å arranged in chains along the C_R axis. Each V-atom occupy the corner or center positions, and octahedrally coordinated with six oxygen ions. The space group of high-temperature VO₂ belongs is P42/mnm (136)⁵. In the insulating phase below T_{MIT} , the crystallographic configuration of VO₂ (Figure. S1b) is a distorted rutile structure, with the unit cell doubling compared to rutile type VO₂⁴. Two different V–V distances of ~ 3.12 and ~ 2.65 Å between the nearest vanadium atoms form the zigzag atom chains⁴, The space group of insulating phase VO₂ is P21/C(14)⁶. The lattice structure of thin-film VO₂ is easily affected by the substrate⁷. Our VO₂/TiO₂(001) film exhibits a tetragonal phase (main text Figure. 1a) in its insulating phase due to the epitaxial stress along the a/b plane⁸.

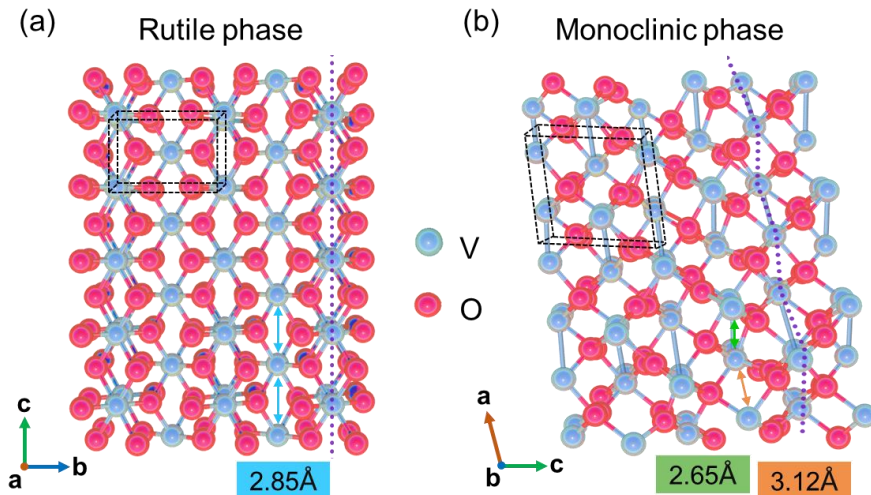


Figure. S1. Crystallographic configuration of the respective phases in VO₂ single crystal sample. (a) Metallic rutile phase. (b) Insulating monoclinic phase.

1.2 Sample Preparation

VO₂ films of thickness 28 nm were synthesized on TiO₂ (001) substrates by pulsed laser deposition (PLD). The rutile TiO₂ substrate is chosen as an ideal substrate for VO₂ film growth due to its stable thermal properties and similar lattice parameters. Deposition process of the VO₂ films on the TiO₂ (001) substrates take place at an optimized pressure and temperature of 10 mTorr and 673 °C, respectively with a pulse laser repetition rate of 5 Hz and a laser fluence of ~1.2 J/cm².

1.3 Crystalline Quality Characterization of VO₂ (High-resolution X-ray Diffraction, Electron Transport Measurements and Atomic Force Microscopy)

Vanadium oxides exist in multiple structural phases, tetravalent vanadium dioxide (VO₂) is the phases which can be readily oxidized to or reduced. $\theta-2\theta$ X-ray Diffraction (XRD) characterization is therefore conducted on the VO₂/TiO₂ film to determine their phase and crystallographic orientation. The diffraction peaks of sample are aligned with the standard tetragonal-like phase (tetragonal-like phase is a distorted by monoclinic phase⁸) of VO₂ and rutile phase of TiO₂, respectively. Subsequently, the Full Width at Half Magnitude (FWHM) obtained from the rocking curves (Figure. S2) can determine the crystalline quality of the VO₂ films. The FWHM data is fitted via using Gauss model, thus the FWHM of the fitted VO₂(002) reflection peak is 0.259 °.

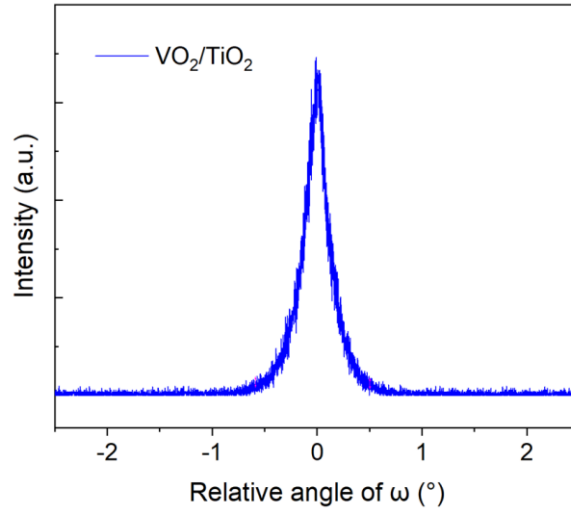


Figure. S2. X-ray rocking curve measurement on VO₂/TiO₂ film.

The electron transport data were taken using the standard four-probe method in a commercial Quantum Design physical property measurement system (PPMS). The transport measurements in our study focused on the metal-insulator transition properties of VO₂. The MIT temperature and temperature-dependent resistivity of the VO₂ film (main text Figure. 1c) are once again in very good agreement with transport measurements involving similar VO₂ film systems^{7, 9-11}. The resistivity of VO₂ film is measured to be $5.9 \times 10^{-4} \Omega \cdot \text{cm}$ in the metallic phase at 400 K. The resistivity value increases by three orders of magnitude as temperature decreases into the insulating phase. The resistivity of VO₂ film is $9.9 \Omega \cdot \text{cm}$ at 250 K. The resistivity of VO₂ increases as temperature decreases. Given the measurement limitations of the instrument, the resistance of the VO₂ film may surpass the instrument's range during transport measurements conducted below ~ 211 K. As shown in the inset of Figure 1c, the MIT temperature (T_{MIT}) of VO₂ film during the heating cycle is ~ 323.3 K. Meanwhile, the MIT takes place at ~ 314.7 K during the cooling process with a small thermal hysteresis width of ~ 8.6 K. VO₂/TiO₂ sample with an abrupt one-step transition by four orders of magnitude further affirms that our VO₂ sample meet the optical experimental requirements. Generally, there is no obvious MIT phase transition in VO₂ films with large amount of oxygen vacancies (Figure S3).

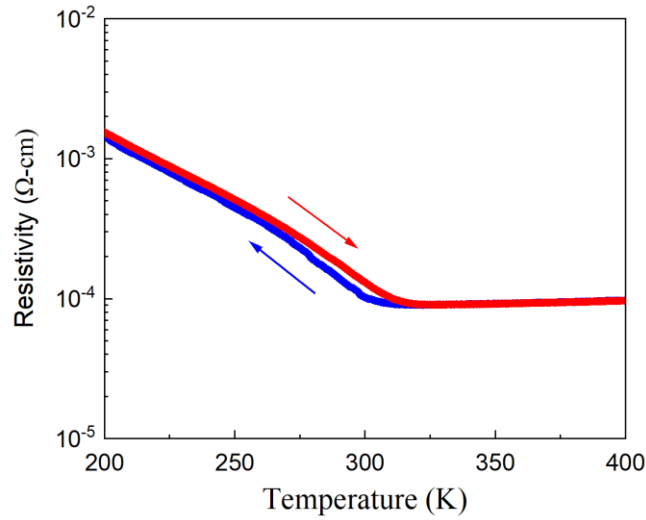


Figure. S3. Transport measurement of VO₂ film with large amount of oxygen vacancies.

The surface morphology of the VO₂/TiO₂ film was measured via atomic force microscopy (AFM). The surface roughness of the VO₂/TiO₂ film is 0.48 nm, which shows that our deposited VO₂ film has homogeneous grains and its surface is very flat and smooth (Figure S4).

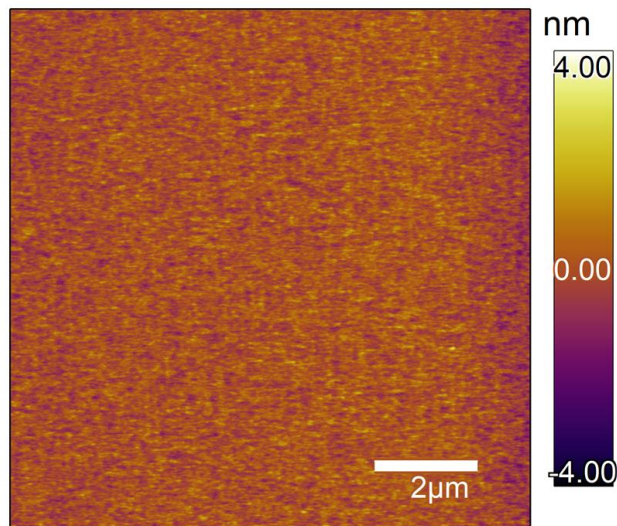


Figure. S4. AFM image of VO₂ film with a roughness of 0.48 nm.

2. Temperature-dependent Spectroscopic Ellipsometry

Measurements

2.1. Experimental Principle and Methods

High-resolution spectroscopic ellipsometry (SE) technique offers extensive coverage across a wide optical energy range. Coupled with its capacity for temperature- and angle-dependent measurements, it proves to be a valuable technique for the identification and examination of quasi-particle excitations across a diverse array of materials¹²⁻¹⁴. Spectroscopic ellipsometry technique also proves highly beneficial as it enables the analysis of interactions between electrons and lattice, a phenomenon stemming from photon excitation, through the elucidation of optical spectra. With the above consideration, SE is a crucial tool to study the optical properties of films¹⁵. Particularly, SE is advantageous for its non-destruction, high sensitivity, and comprehensive response, suitable for the characterization of strongly-correlated system, such as VO₂ films^{16, 17}. Without rely on a Kramers-Kronig transformation, SE can directly estimate the complex elements of the dielectric tensor from a single measurement. Using this method, SE can be extremely sensitive to charge distributions of surface properties¹⁸. The Schematic illustration of the spectroscopic ellipsometry experimental measurements as shown in Figure. S5.

Spectroscopic ellipsometry (SE) measurements are conducted using a custom-made J. A. Woollam Co., Inc Variable Angle Spectroscopic Ellipsometer (VASE) in the photon energy range of 0.5-6.0 eV at incident angle of 70° with respect to the plane normal. Measurements are conducted at temperatures between 100 K and 400K in a high-vacuum chamber at a base pressure of $\sim 10^{-9}$ mTorr. SE measurements measure the ellipsometric parameters Ψ (amplitude ratio between p- and s- polarized reflected light) and Δ (phase difference between of p- and s-polarized reflected light). The dielectric coefficients and optical conductivity of the VO₂/TiO₂ films are extracted from the ellipsometric parameters Ψ and Δ utilizing an air/VO₂/TiO₂ multilayer model.

We measured the ellipsometric parameters Ψ (amplitude ratio between p- and s-polarized reflected light) and Δ (phase difference between of p- and s-polarized

reflected light). The dielectric coefficients and optical conductivity of the VO₂/TiO₂ films are extracted from the ellipsometric parameters Ψ and Δ utilizing an air/VO₂/TiO₂ multilayer model, where the VO₂ film consists of an average homogeneous and uniform medium.

Ellipsometric parameters Ψ and Δ are defined as

$$\tan \Psi \exp(i\Delta) \equiv \frac{r_p}{r_s} \quad (\text{S1})$$

Where r_p and r_s represent the reflectivity of p- and s- polarized light. Combined with the Fresnel equations, these variables are expressed as

$$r_p^{ij} = \frac{n_j \cos \theta_i - n_i \cos \theta_j}{n_j \cos \theta_i + n_i \cos \theta_j} \quad (\text{S2})$$

and

$$r_s^{ij} = \frac{n_j \cos \theta_i - n_i \cos \theta_j}{n_j \cos \theta_i + n_i \cos \theta_j} \quad (\text{S3})$$

Where n and θ is the refraction index and incident angles with respect to the plane normal respectively. Here, i and j are viewed as two materials. The complex dielectric function $\varepsilon(\omega) = \varepsilon_1(\omega) + i\varepsilon_2(\omega)$ of media can be obtained by

$$N^2 \equiv \varepsilon \quad (\text{S3})$$

where ω represent the photon frequency.

In typical two layers thin-film: VO₂ film on TiO₂ substrate, the reflectivity can be expressed as follows

$$r_{multi} = \frac{r_{vac, film} + r_{film, sub} \exp(i2\delta_{film})}{1 + r_{vac, film} \cdot r_{film, sub} \exp(i2\delta_{film})} \quad (\text{S5})$$

where

$$\delta_{film} = \frac{2\pi d_{film}}{\lambda} n_{film} \cos \theta \quad (\text{S6})$$

where the subscripts multi and vac represent VO₂ film on TiO₂ substrate multilayer system and the vacuum, respectively. δ_{film} is the change in light phase as it reflects from the VO₂ film, λ denotes the light wavelength, and d_{film} is the thickness of the VO₂ film grown by PLD. As for the refractive index of the substrate, one clean bulk TiO₂ was measured by the spectroscopic ellipsometry.

After measuring complex dielectric function of TiO₂ substrate, the complex dielectric function of VO₂ films can be extracted from Ψ and Δ through fitting with Drude-Lorentz oscillators according to

$$\tilde{\varepsilon}(\omega) = \varepsilon_{\infty} + \sum_{k=1}^n \frac{\omega_{pk}^2}{\omega_{0k}^2 - \omega^2 - i\gamma_k \omega} \quad (S7)$$

$$\tilde{\varepsilon}(\omega) = \varepsilon_1(\omega) + i\varepsilon_2(\omega) \quad (S8)$$

where ω_0 is the oscillator frequency, ω_p is the plasma frequency, γ is the line-width. ε_{∞} is represent the higher-frequency oscillators.

Subsequently, the real part of the optical conductivity σ_1 can be calculated with the following equation¹⁹:

$$\sigma_1 = \omega \cdot \varepsilon_0 \cdot \varepsilon_2 = \frac{E}{\hbar} \cdot \varepsilon_0 \cdot \varepsilon_2 = \frac{2\pi\varepsilon_0}{h} \cdot E \cdot \varepsilon_2 \quad (S9)$$

where ω is the frequency of photon, E is the energy of photon, ε_2 is the imaginary part of the dielectric function, ε_0 is a constant which is approximately equal to 8.85×10^{-12} F/M, \hbar is also a constant, after unit conversion, the value is about 4.14×10^{-15} eV·s.

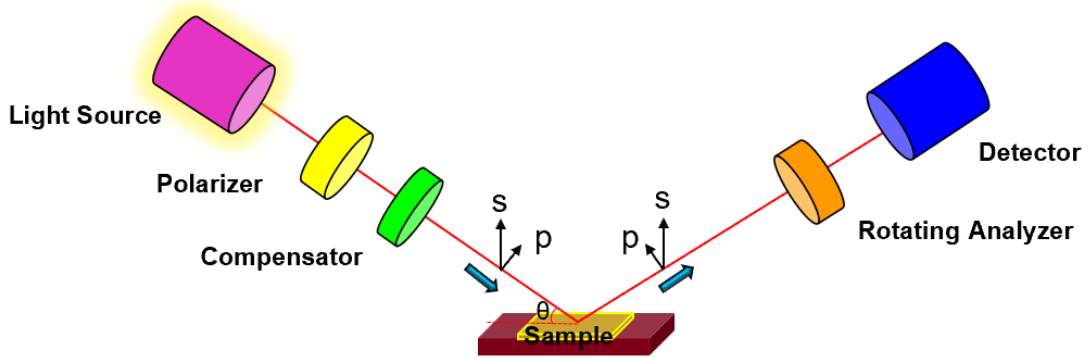


Figure. S5. Schematic of spectroscopic ellipsometry with the respective optical components.

2.2 Temperature-dependent Spectroscopic Ellipsometry Characterization

Spectroscopic ellipsometry represents a highly versatile tool for probing and effectively distinguishing between conventional optical band transitions and quasiparticle dynamics that arise due to many-body effects in strongly-correlated materials. It is thus widely utilized to establish the optical response and electron structures in a wide range of condensed matter systems and strongly-correlated materials at the nanoscale¹²⁻¹⁴. Detailed optical characterization of quasiparticles was conducted on VO₂/TiO₂ film using spectroscopic ellipsometry at temperatures between 100 K and 400 K where the MIT takes place. Optical responses of the VO₂ film were collected with incident photon energy between 0.5 and 6.0 eV. With the transport measurements confirming the MIT phenomena of the VO₂ film during the heating and cooling processes, it behaves as an insulator with a band gap (~ 0.6 eV) below 323.3 K (T_{MIT})^{20, 21}. It then transforms into a rutile metal at temperatures above 323.3 K²². These transport properties have been confirmed by the optical characterization using spectroscopic ellipsometry with prominent changes to the optical parameters caused by the transition process especially with regards to its energy bands and quasiparticle dynamics in both the metallic and insulating states. In the spectroscopic ellipsometry measurements, we observe the traces of three types of quasiparticles excitations, small polarons, metallic plasmons and

correlated plasmons, respectively. The presence of polaron state related to small polarons is detected by analyzing the σ_1 absorption peaks in the insulating state. Meanwhile, metallic plasmons and correlated plasmons are found to distribute in the loss-function spectra.

2.3 The Number of Effective Carriers

The number of effective carriers per formula unit [$N_{eff}(\omega)$] is as follows:

$$N_{eff}(\omega) = \frac{2m_0V}{\pi e^2} \int_{w_2}^{w_1} \sigma_1(\omega') d\omega' \quad (S10)$$

As shown in Figure. S6, the reduction of $N_{eff}(\omega)$ in region I as temperature decreases is closely accompanied by the enhancement of $N_{eff}(\omega)$ in in regions II, III, IV, V. The changes of spectral weight and the number of the effective carriers are consistent with the conductivity behavior, indicating the occurrence of the MIT process. This is also an important sign of strong electronic correlations²³.

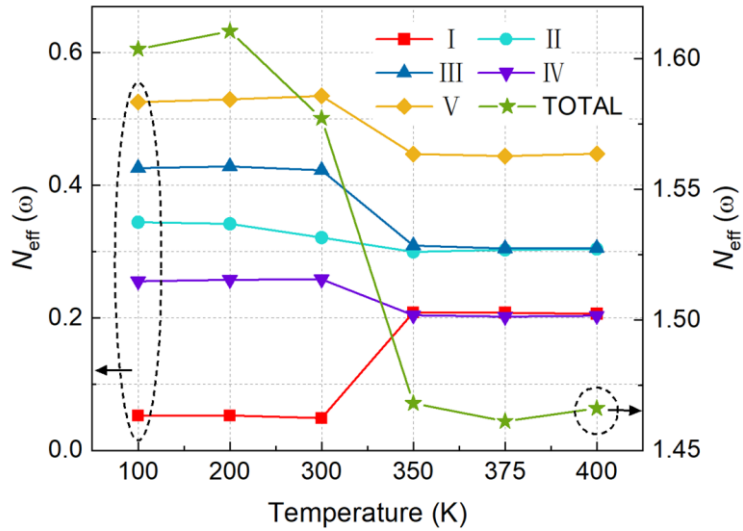


Figure. S6. The number of the effective carriers per formula unit [$N_{eff}(\omega)$] as a function of temperature for different spectral regions: I (0-1.62 eV), II (1.62-3.28 eV), III (3.28-4.10 eV), IV (4.10-4.72 eV), (4.72-6.0 eV) and total (0-6.0 eV).

2.4. Drude-Lorentz Model

The dielectric functions of metals and semiconductors with high carrier concentrations exhibit strong free carrier absorption characteristics, which can be represented by the Drude model. The carrier concentration and mobility in metals/semiconductors can be estimated using the Drude model for analysis. However, there are two contributions in both ε_1 and ε_2 spectrums of metals/semiconductors in reality, free-carriers and bound electrons. Therefore, the dielectric function of a metal/semiconductor is expressed as

$$\tilde{\varepsilon}(\omega) = \varepsilon_1(\omega) + \varepsilon_2(\omega) \quad (\text{S11})$$

$$\tilde{\varepsilon}(\omega) = \tilde{\varepsilon}_{free}(\omega) + \tilde{\varepsilon}_{bound}(\omega) \quad (\text{S12})$$

The free electron component as represented by $\tilde{\varepsilon}_{free}$ is modelled by the Drude model while the bound electrons as represented by $\tilde{\varepsilon}_{bound}$ by the Lorentz model. This component is introduced to analyze the relationship between the dielectric polarization phenomenon and the applied electromagnetic field to assist in modelling the dielectric property of the system.

Hence, the Drude-Lorentz model has been used for in modelling the dielectric functions of several semiconducting systems which possess both free and bound electronic properties. It easily models the dielectric properties of such systems over a wide spectral range and provide the perfect Gaussian line shape for the construction of optical curve fitting ²⁴.

2.5 Optical Transitions Analysis in Optical Conductivity Spectra

In the metallic phase at 400 K, anti-ferroelectric displacement along the [110] direction decreases the p - d hybridization, causing the π^* band to shift downward towards the Fermi level ^{5, 25}. As a result, there are two half-filled bands, $d_{||}$ and π^* located at the Fermi level in the metallic state. Three features in the σ_1 spectra can be attributed to optical transitions between occupied energy bands and unoccupied energy bands ²⁶. Combining with our analysis of spectroscopic ellipsometry, feature α (~ 2.75 eV) can

be attributed to the optical transition from the filled O $2p$ band to the half-filled $d_{||}$ band, while a weak shoulder feature β (~ 3.38 eV) is ascribed to the optical transition from the filled O $2p$ band to the half-filled π^* band. Meanwhile, feature γ (~ 5.07 eV) is attributed to the optical transition between half-filled $d_{||}$ band and empty σ^* band.

Abrupt MIT occurs at 323.3 K, leading to significant changes in both the electrical conductivity and lattice structure. We aim to account for these optical conductivity features by comparing our results to earlier theoretical and experimental studies ^{27, 28}. In the insulating phase at 100 K, previously studies revealed that the energy band of VO₂ evolves with temperature ²⁹, specifically, the energy bands near the Fermi level shift closer to it with increasing temperature. This reduces the energy difference between the minimum conduction band and maximum valence band. The optical conductivity data of insulating VO₂ film shows the feature labelled A is situated at ~ 1.26 eV at 100 K which redshifts to ~ 1.16 eV at 300 K. This feature can be attributed to the optical transition between adjacent energy bands that near the Fermi level that is commonly reported in the insulating state ^{30, 31}.

The Lower Hubbard band (LHB) and Upper Hubbard band (UHB) are two subbands split by half-filled Hubbard model due to the influence of Hubbard intra-atomic Coulomb repulsion energy ²⁶. LHB is a full-filled energy band which located below the Fermi level while the UHB is an empty energy band which located above the Fermi level and near the π^* bands ²⁹. Hence, feature C at ~ 3.39 eV in the insulating phase can be attributed to the interband transition between the LHB and UHB ^{25, 31}, revealing strong Peierls charge-density wave ordering from dimerization in insulating VO₂ ^{17, 32}. In the energy regions away from the Fermi level. The hump feature E at ~ 5.33 eV with high-intensity spectral weight in insulating state can be defined as the transition from the O $2p$ bands to the empty π^* band and from LHB to empty σ^* band ^{30, 33}.

2.6 Plotting the Differential Spectra of the Optical Conductivity

A more in-depth analysis of the spectroscopic ellipsometry data is conducted and they are plotted in the form of a differential spectra of optical conductivity between various temperatures and the 300 K in insulating state, $\Delta\sigma_1(\omega, T) = \sigma_1(\omega, T) - \sigma_1(\omega, 300 \text{ K})$, as shown in Figure S7. We now focus on the low-energy region (0.5 eV—2.0 eV). An independent feature can be observed at $\sim 0.7 \text{ eV}$ across different temperatures. This feature may be attributed to the optical transition from the polaron state to the π^* band.

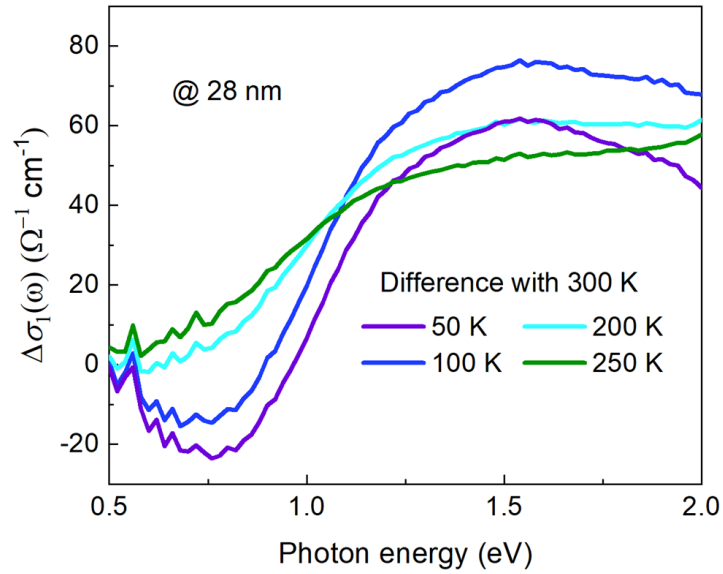


Figure S7. The differential spectra of the optical conductivity for 28nm-VO₂/TiO₂ film.

The same situation is also observed in the 27.0 nm-VO₂/TiO₂ films. A set of optical conductivity and differential spectra of the 27-nm VO₂ film is displayed in Figure S8. At the lower energy position of $\sim 0.7 \text{ eV}$, an optical transition feature is also observed and it can also be attributed to the emergence of the polaron state.

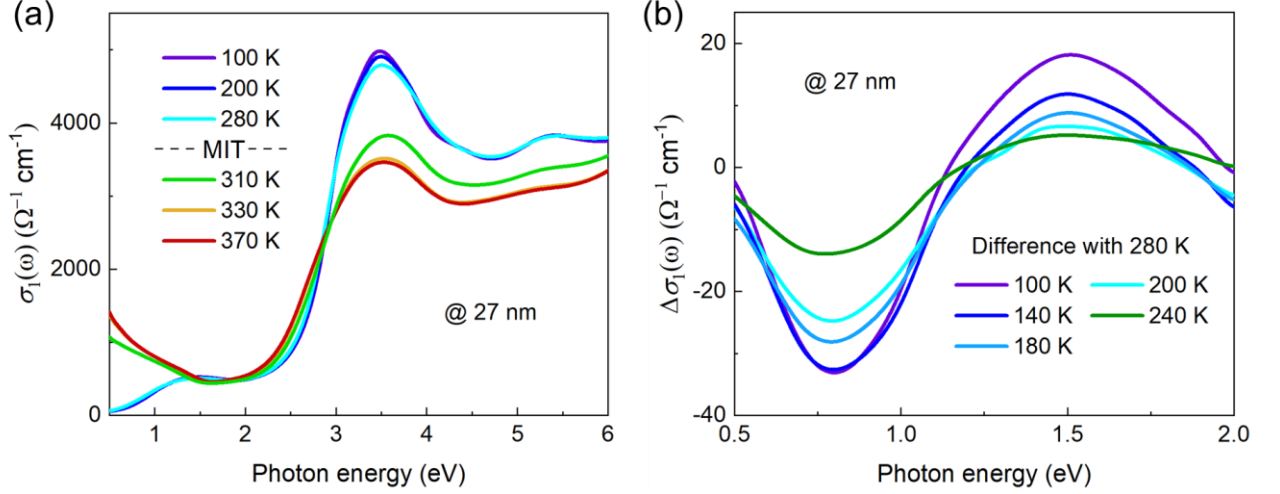


Figure S8. (a) σ_1 spectra of 27nm-VO₂/TiO₂(001) film from 0.5 to 6.0 eV at the respective temperatures in both its insulating and metallic phases. (b) Differential spectra of optical conductivity for 27nm-VO₂/TiO₂ film.

2.7 Dynamical Response Loss-Function

Further insights to the loss-function(LF) between the metallic and insulating vanadium dioxide systems which can successfully describe the difference between the electron behaviors of VO₂ around T_{MIT} ³⁴. In a broader sense, the dynamic energy loss measurement technique can lay a foundation for the analysis of the optical properties in VO₂ and other phase change materials ^{35, 36}.

The optical LF is further derived with the spectra from the dielectric function based on the following expression:

$$LF = Im\left(-\frac{1}{\tilde{\epsilon}}\right) = \frac{\epsilon_2}{\epsilon_1^2 + \epsilon_2^2} \quad (S13)$$

where ϵ denotes the complex dielectric function ($\tilde{\epsilon} = \epsilon_1 + i\epsilon_2$).

2.8 The Observation of Plasmon Excitations

To further analyze the quasiparticle features and opto-electronic properties of the VO₂ system and distinguish between the insulating and metallic phases, the optical loss-

function (LF) is further derived with the spectra displayed in main text Figures. 3(g-h). Metallic phase VO₂ shows clear metallic behavior with the prominent Drude response in σ_1 (main text Figure. 2a) and zero-crossing of ε_1 (main text Figure. 3g) at ~ 1.10 eV at 350 K. This zero-crossing blueshifts monotonically to ~ 1.12 eV at 400 K – near the energy position of loss-function peak A₁ (main text Figure. 3h) marking the presence of metallic plasmons (peak A₁) attributed to the collective excitation of free charges³⁵. While the coincidence of the zero-crossing in the ε_1 spectra and the LF peak A₁ at the same photon energy position marks the presence of metallic plasmons in metallic phase VO₂, note the very slight disparity in the respective energy position as shown in Figures. 3(g-h) where it can be attributed to the presence of free electron scattering in the VO₂ crystalline system³⁷. Since VO₂ exhibits metallic behavior at temperatures above T_{MIT} , metallic plasmons can also be detected. Our detection of metallic plasmons is in complete agreement with previous literature report³⁸⁻⁴⁰. Figure. S9 shows the peak positions of metallic plasmons (peak A₁) present obvious temperature-dependent properties. This is related to the temperature-dependence of concentration of charge carriers in the metallic state⁴¹.

Correlated plasmons present in strongly-correlated systems have been reported in a diverse class of materials⁴²⁻⁴⁴. VO₂ is a quintessential strongly-correlated system, using methods similar to those employed in previous studies^{42, 45}, we have successfully detected correlated plasmons in VO₂. An essential observation is depicted in the ε_2 and LF spectra of VO₂ [main text Figures. 3(i-j)]. An essential observation is depicted in the ε_2 and LF spectra of VO₂ (Figures 3i,j). In the metallic phases (400 K), apart from the Drude peaks (A₁), several features, namely B₁, B₂ and B₃ can be observed in the LF spectra. Notably, the energy positions of features B₁, B₂ and B₃ in the LF spectra closely align with those of another group of three features in the ε_2 spectra: B₁' , B₂' and B₃' , respectively. In the insulating state (100 K) of LF, several features, namely C₁, C₂, C₃, C₄ and C₅ also correspond one-to-one with the features in ε_2 (features C₁' , C₂' , C₃' , C₄' and C₅'). These observations suggest that the simultaneous presence in both the ε_2 and

LF spectra where they indicate a coupling between optical and plasmonic excitations in metallic and insulating VO₂⁴² (Supplementary, Section 2.7). Therefore, features B₁, B₂ and B₃ in the metallic phase and C₁, C₂, C₃, C₄ and C₅ in the insulating phase VO₂ can be regarded as a form of correlated plasmons, arise from the collective excitations of correlated electrons.

The observation and characterization of both conventional (metallic) and correlated plasmons in the distinct phases of the VO₂ film offer valuable insights into the evolution of collective charge dynamics within the system as it undergoes transformations between structural and electronic phases. Furthermore, a comprehensive understanding of the plasmonic properties in VO₂ is crucial for their utilization in optoelectronic devices.

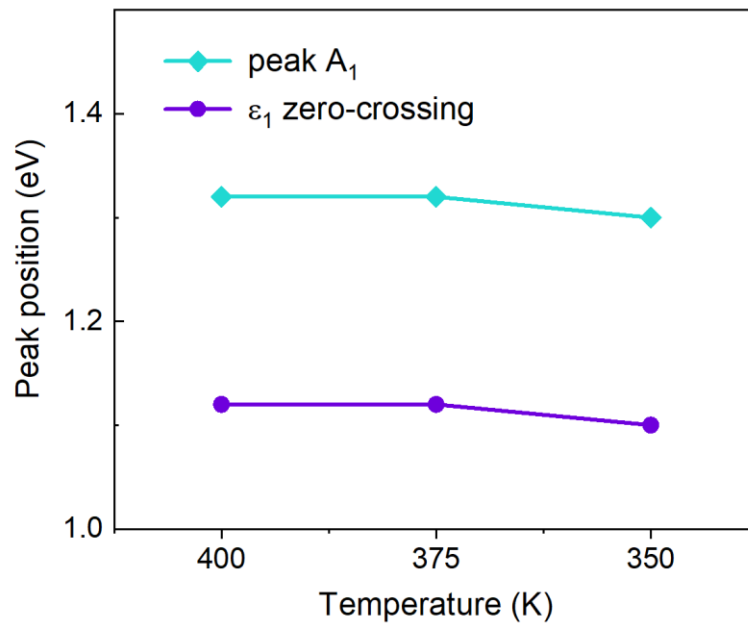


Figure. S9. The slight disparity of the position relationship between zero-crossings of ϵ_1 and peak A₁ can be attributed to electron scattering in the system.

3. Small Polarons Analysis

3.1 The Characteristics of Small Polarons

In a multidimensional system, the discernment between large polarons and small polarons serves as a crucial aspect in the realm of quasiparticles. These two distinct types of quasiparticles exhibit dissimilar effects on electron structures and optical transitions⁴⁶⁻⁴⁸. Large polarons, in particular, tend to induce a significant renormalization of the band gap, whereas small polarons, being more extensively spread across adjacent unit cells, may introduce discrete mid-gap states⁴⁹. In light of our findings regarding the insulating σ_1 spectra (main text Figure. 2e), only a solitary mid-gap state emerges. Hence, we contend that the polarons observed in the VO₂ system under investigation can be classified as small polarons.

The localized interaction between excess electrons and the V lattices is responsible for the emergence of short-range effects. The local lattice undergoes relaxation in the vicinity of the V site, thus accompanying the creation of small polarons within the insulating state^{50,51}. These small polarons, propelled by the short-range electron-lattice interaction^{52,53}, trigger electron transitions from a self-trapped ground state to adjacent localized states^{50,51,54,55}. Moreover, the presence of small polarons disrupts the magnetic moment and leads to an elongation of the V-O bond length, thereby imbuing the insulating phase of VO₂ with spatial anisotropy and orbital polarization⁵⁶. Therefore, our investigation signifies that the formation of small polarons in VO₂ originates from the interplay between electrons and the lattices, giving rise to electron polaron state in close proximity to the valence band.

Another important discovery to note is that V⁴⁺-V⁴⁺ dimerized pairs are formed in its insulating state^{55,57-59} where the V⁴⁺ oxidation state is an essential condition for the formation of small polarons in VO₂^{60,61}. Meanwhile, the presence of V³⁺ and V⁵⁺ states in metallic state VO₂ does not favor the formation of small polarons⁶². This accounts for the presence of small polarons in insulating state VO₂ while it is absent from its metallic phase, which is consistent with both the optical and transport analyses of the main text.

3.2 Small Polaron Hopping Model

The electrical conductivity of the system exhibits a linear temperature-dependence, as indicated by the relationship $\ln(\sigma T^{3/2}) \sim T$. This behavior takes into account the impact of lattice vibrations on the resonance integral^{63, 64}. To describe the contribution of hopping to the electrical conductivity, the Small polaron hopping model proposed by Bryksin⁵³ is employed.

The hopping conductivity demonstrates a temperature dependence that can be expressed by the following relation:

$$\ln(\sigma T^{3/2}) = A + \frac{k_B T}{\varepsilon} - \frac{E_a}{k_B T} \quad (\text{S14})$$

where A is the constant that independent of temperature, K_B is the Boltzmann constant, ε is the vibrational energy scales and E_a is the small polarons hopping activation energy.

The electronic transport mechanism observed in the VO_2 system suggests that the thermal lattice vibrations' magnitude influences the ability of small polarons to hop between lattice sites, thereby affecting the system's electrical conductivity⁶³. In the low-temperature phase, the conductivity primarily arises from the hopping of small polarons. Notably, the experimental data have been fitted to match the curvature that is in line with the theoretical and experimental results below T_{MIT} . An activation energy (E_a) for small polaron hopping of 2.636×10^{-2} eV can be derived, along with a lattice vibrational energy (ε) of 1.95×10^{-3} eV, consistent with earlier investigations of VO_2 ^{63, 64}. However, a significant deviation between the hopping conductivity of small polarons and the experimental conductivity arises just before and during the onset of the MIT. The $\ln(\sigma T^{3/2})$ relationship in the metallic regime exhibits a substantially steeper rise compared to the expectations from the small polaron hopping model.

3.3 Small Polaron State

Having provided experimental evidence that small polarons are present in the insulating state VO₂ based on a detailed analysis of the transport data below and above the metal-insulator transition temperature, it is essential to clearly attribute features B and D observed in the optical spectra (Figure. 2e) to the presence of the polaron state in insulating phase VO₂. A previous theoretical study has indicated that polaron state is formed at energy region in the order of ~1 eV below the conduction band minimum (CBM) in large bandgap oxide systems⁴⁹. With the relatively small bandgap of insulating VO₂ of ~ 0.67 eV, not only is the formation of the small polaron state at 0.6 eV below the empty π^* band at 100 K (main text Figure. 4b) theoretically consistent, but it also agrees with experimental detected polaron state in other small bandgap oxide system⁴⁶.

3.4 Analysis for The Band Structures

As previously discussed, feature B in the optical conductivity spectra has been associated with the optical transition from the polaron state to the Upper Hubbard band (UHB), while feature D corresponds to the optical transition from the polaron state to the σ^* band. Interestingly, the energy positions of both features B and D in the optical conductivity spectra, as shown in Figures. S10a-b, exhibit no significant changes within the temperature range from 100 K to 300 K. This suggests that there is also a corresponding position shift within the temperature changing in the polaron band along with the UHB and σ^* band. Hence, the relative energy differences between these bands remains unchanged as seen in the positions of features B and D.

In order to analyze the unoccupied V-3d conduction bands in insulating VO₂ film at temperatures below the MIT ($T < T_{MIT}$), X-ray Absorption Spectroscopy (XAS) was performed on the O-K edge^{65, 66}. Figure. S10c presents the XAS results from Ref⁶⁷, which exhibit two prominent maxima at ~ 529.5 eV and ~ 532.0 eV. These peaks can be attributed to the transition from the O 1s state to the hybridized O 2p state with the

unoccupied conduction bands π^* and σ^* , respectively⁶⁸. Notably, the feature observed at ~ 530.5 eV is only present below T_{MIT} ⁶⁷ and can be considered as the UHB feature.

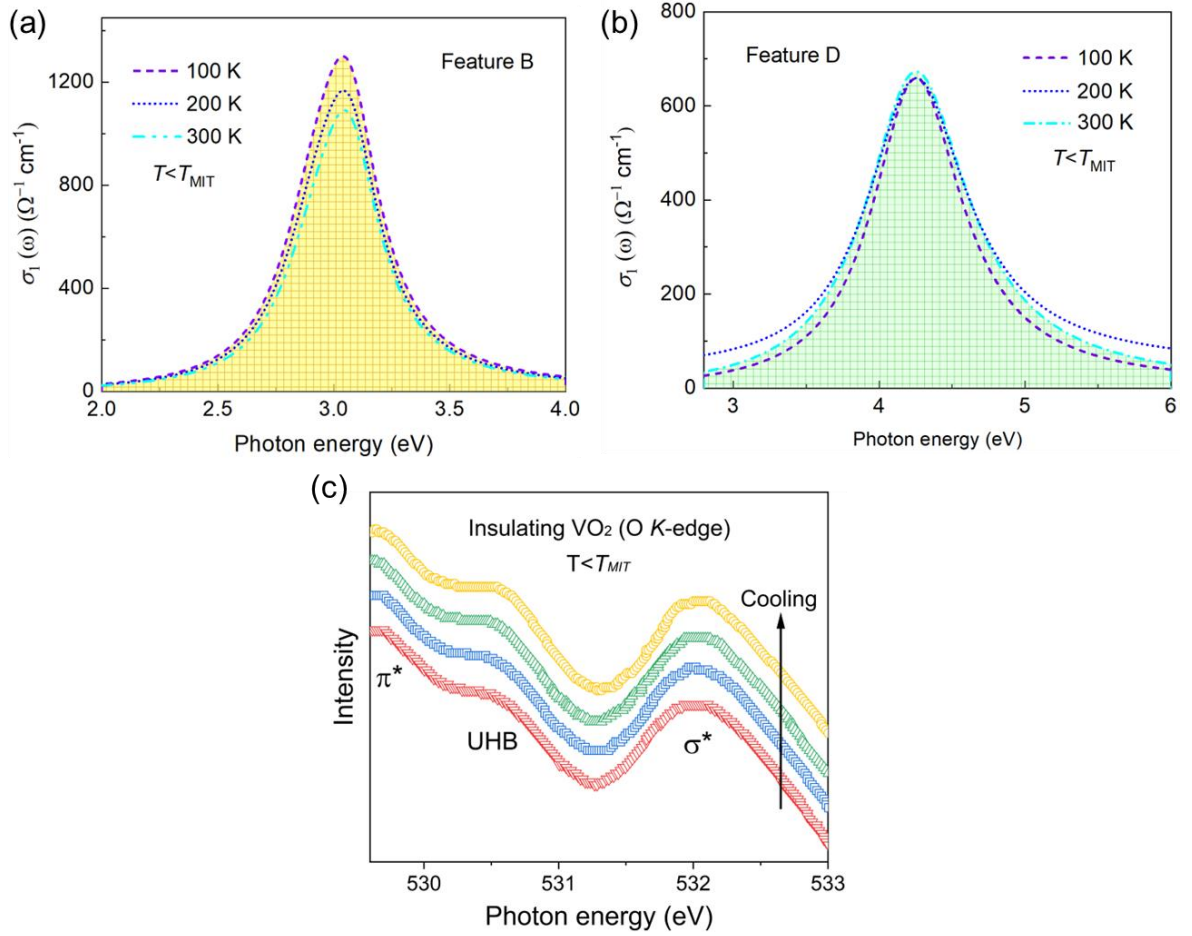


Figure. S10. The characteristics of peak B & D and O-K edge spectra elucidated from XAS measurements. (a-b) The optical conductivity of fitting features B and D (always located at ~ 3.02 eV and ~ 4.26 eV, respectively) in the insulating state at the temperature range from 300 K to 100 K. (c) Temperature dependence analysis of O-K edge in the XAS spectra is measured from Ref⁶⁷.

4. First-principles Calculations

Hence, by comparing evidences from our optical studies with previous theoretical studies detailing the presence of the polaron state in insulating phase VO₂, they provide substantial evidences that a small polaron state is present below the Fermi level with features B (~ 3.39 eV) and D (~ 4.26 eV) in the σ_1 spectra (main text Figure 2e) being

the optical transitions from the polaron state to the UHB and σ^* band, respectively. While our experimental studies have provided very conclusive evidences pointing to the presence of small polarons in insulating phase VO₂, further confirmation of this quantum quasiparticle will be made via a set of computational study as discussed thereafter.

Density functional theory (DFT) calculations were conducted using the Vienna ab initio Simulation Package (VASP) with the projector augmented-wave method. The Perdew-Burke-Ernzerhof (PBE) parameterized Generalized Gradient Approximation (GGA) has been adopted for the ion-electron interaction and the exchange-correlation interaction, respectively⁶⁹⁻⁷². A plane wave basis with a kinetic energy cutoff of 600 eV was used to expand the electronic wavefunction. The valence states considered are O $2s^2 2p^4$ and V $3s^2 3p^6 3d^4 4s^1$. The Γ -centered k -point grid was set to $11 \times 11 \times 9$ and $5 \times 5 \times 4$ for the VO₂ unit cell and the $2 \times 2 \times 2$ supercell, respectively. The total energy convergence criterion is 1.0×10^{-5} eV and the structural relaxation was conducted until the force on each atom is less than 0.01 eV/Å. A Hubbard U value of 5.3 eV has been applied to the V $3d$ electrons to reproduce the experimental band gap of the insulating phase of VO₂⁷³. The $2 \times 2 \times 2$ supercell containing 96 atoms was used to simulate the (non-)polaronic state. For the polaronic state simulation, in particular, one vanadium site was slightly displaced from its equilibrium position in order to break the symmetry constraint, whereas there is no such an initial displacement for the non-polaronic state simulation. This method has been widely used to study polarons in various oxide materials⁷⁴⁻⁷⁷. In particular, the value for Hubbard U of 5.3 eV on the V $3d$ electrons adopted has been carefully selected in order to accurately describe the property of interest and the experimental band gap of the insulating VO₂⁷⁷⁻⁷⁹. With the focus on the electronic structure of insulating VO₂ and its metal-insulator transitional properties, the value of U has been fitted to reproduce the band gap size of the insulating VO₂ (Experiment: ~ 0.67 eV (100 K); DFT+ U : 0.601 eV). With the ability of the DFT+ U approach to accurately describe the polaron state and provide important insights to the

experimental observations in strongly-correlated systems^{48, 80-82}, the consistent results between the band structure calculations and the experimental findings and that they agree with previous studies are clear indications that the observation of small polarons in insulating phase VO₂ is reliable and accurate. Moreover, it is noted that, to the best of our knowledge, neither the standard DFT method nor its advanced derivative methods can simultaneously and properly describe the magnetic and electronic properties of strongly correlated VO₂ systems⁸³. We also note that no magnetism was experimentally observed in our samples. Therefore, the spin degree of freedom has not been considered throughout the DFT calculations. This is to circumvent the spurious effect induced by magnetism. As such, two electrons were added to the 2×2×2 supercell during the (non-)polaronic state simulation, namely, one electron for each degenerate spin channel. Similar approaches have been recently adopted to investigate other phases of vanadium oxides⁷⁷.

Meanwhile, these localized electrons can also be found in neighboring vanadium sites in the vicinity where the polaron states are formed (37). This is a clear indication that it is energetically more favorable for the excess electrons to be localized in the V lattice sites to form small polarons than in the non-polaron state where the electrons are homogeneously distributed across the lattice system. As compared to the non-polaron state counterpart, while the charge trapping at the V lattice site further increases the long V-V distance, the short V-V distance remains virtually unchanged. This is likely due to the aforementioned charge transfer from that neighboring V site. The calculated band gap is 0.601 eV, in agreement with that previously reported for the insulating phase of VO₂^{20, 21}.

This polaron state emerged below the Fermi level in the polaron state and it mainly consists of the Vt_{2g} states. Very importantly, the results of these DFT studies show clear consistency with our experimental findings. Specifically, the mid-gap state that emerged in the visualized PDOS can be attributed to the formation of the polaron

state. This provides compelling evidence to substantiate our experimental results for the presence of small polarons in insulating state VO₂.

References

1. T. Yao, et al. Understanding the nature of the kinetic process in a VO₂ metal-insulator transition. *Phys Rev Lett* **105**, 226405 (2010).
2. K. Han, et al. Enhanced Metal-Insulator Transition in Freestanding VO₂ Down to 5 nm Thickness. *ACS Appl Mater Interfaces* **13**, 16688-16693 (2021).
3. A. Cavalleri, T. Dekorsy, H. H. W. Chong, J. C. Kieffer & R. W. Schoenlein Evidence for a structurally-driven insulator-to-metal transition in VO₂: A view from the ultrafast timescale. *Phys. Rev. B* **70**, 161102 (2004).
4. Y. Huang, et al. Phase transition analysis of thermochromic VO₂ thin films by temperature-dependent Raman scattering and ellipsometry. *Applied Surface Science* **456**, 545-551 (2018).
5. N. B. Aetukuri, et al. Control of the metal-insulator transition in vanadium dioxide by modifying orbital occupancy. *Nat. Phys* **9**, 661-666 (2013).
6. J. Wei, H. Ji, W. Guo, A. H. Nevidomskyy & D. Natelson Hydrogen stabilization of metallic vanadium dioxide in single-crystal nanobeams. *Nature Nanotechnology* **7**, 357-362 (2012).
7. Y. Muraoka & Z. Hiroi Metal-insulator transition of VO₂ thin films grown on TiO₂ (001) and (110) substrates. *Appl. Phys. Lett* **80**, 583-585 (2002).
8. H. Qiu, et al. The tetragonal-like to rutile structural phase transition in epitaxial VO₂/TiO₂(001) thick films. *New Journal of Physics* **17**, 113016 (2015).
9. N. A. Jaewoo Jeong, Tanja Graf, Thomas D. Schladt, Mahesh G. Samant, Stuart S. P. Parkin Suppression of Metal-Insulator Transition in VO₂ by Electric Field-Induced Oxygen Vacancy Formation. *Science* **339**, 1402-1405 (2013).
10. J. Lee., et al. Isostructural metal-insulator transition in VO₂. *Science* **362**, 1037-1040 (2018).
11. H. Paik, et al. Transport properties of ultra-thin VO₂ films on (001) TiO₂ grown by reactive molecular-beam epitaxy. *Appl. Phys. Lett* **107**, 163101 (2015).
12. X. Yin, et al. Unraveling how electronic and spin structures control macroscopic properties of manganite ultra-thin films. *NPG Asia Materials* **7**, e196-e196 (2015).
13. Z. Q. Li, et al. Dirac charge dynamics in graphene by infrared spectroscopy. *Nat. Phys* **4**, 532-535 (2008).
- 14.
15. X. Yin, et al. Tunable inverted gap in monolayer quasi-metallic MoS₂ induced by strong charge-lattice coupling. *Nat Commun* **8**, 486 (2017).
16. M. M. Qazilbash, et al. Mott transition in VO₂ revealed by infrared spectroscopy and nano-imaging. *Science* **318**, 1750-3 (2007).
17. D. J. Lahneman, et al. Insulator-to-metal transition in ultrathin rutile VO₂/TiO₂(001). *NPJ Quantum Mater* **7**, (2022).
18. X. Yin, et al. Modulation of New Excitons in Transition Metal Dichalcogenide-Perovskite Oxide System. *Adv Sci* **6**, 1900446 (2019).
19. F. J. Wong, N. Hong & S. Ramanathan Orbital splitting and optical conductivity of the insulating state of NbO₂. *Physical Review B* **90**, 115135 (2014).

20. J. Wei, Z. Wang, W. Chen & D. H. Cobden New aspects of the metal-insulator transition in single-domain vanadium dioxide nanobeams. *Nat Nanotechnol* **4**, 420-4 (2009).
21. S. Cheng, et al. Inherent stochasticity during insulator-metal transition in VO₂. *PNAS* **118**, 2105895118 (2021).
22. C. Xu, et al. Transient dynamics of the phase transition in VO₂ revealed by mega-electron-volt ultrafast electron diffraction. *Nat Commun* **14**, 1265 (2023).
23. X. Yin, et al. Modulation of Manganite Nanofilm Properties Mediated by Strong Influence of Strontium Titanate Excitons. *ACS Applied Materials & Interfaces* **10**, 35563-35570 (2017).
24. A. Vial, A.-S. Grimault, D. Macías, D. Barchiesi & M. L. de la Chapelle Improved analytical fit of gold dispersion: Application to the modeling of extinction spectra with a finite-difference time-domain method. *Physical Review B* **71**, 085416 (2005).
25. T. J. Huffman, et al. Insulating phases of vanadium dioxide are Mott-Hubbard insulators. *Physical Review B* **95**, 075125 (2017).
26. M. M. Qazilbash, et al. Electrodynamics of the vanadium oxides VO₂ and V₂O₃. *Phys. Rev. B* **77**, 115121 (2008).
27. J. M. Tomczak & S. Biermann Optical properties of correlated materials: Generalized Peierls approach and its application to VO₂. *Physical Review B* **80**, 085117 (2009).
28. H. W. Verleur, A. S. Barker & C. N. Berglund Optical Properties of VO₂ between 0.25 and 5 eV. *Physical Review* **172**, 788-798 (1968).
29. M. Nazari, et al. Temperature dependence of the optical properties of VO₂ deposited on sapphire with different orientations. *Physical Review B* **87**, 035142 (2013).
30. L. Fan, et al. Revealing the role of oxygen vacancies on the phase transition of VO₂ film from the optical-constant measurements. *RSC Adv* **8**, 19151-19156 (2018).
31. K. Okazaki, S. Sugai, Y. Muraoka & Z. Hiroi Role of electron-electron and electron-phonon interaction effects in the optical conductivity of VO₂. *Phys. Rev. B* **73**, 165116 (2006).
32. S. Kim, et al. Orbital-selective Mott and Peierls transition in H_xVO₂. *npj Quantum Materials* **7**, (2022).
33. W. W. Li, Q. Yu & J. R. Liang Intrinsic evolutions of optical functions, band gap, and higher-energy electronic transitions in VO₂ film near the metal-insulator transition region. *Appl. Phys. Lett* **99**, 241903 (2011).
34. M. Thomas & E. E. Chain Optical properties and electron energy-loss diagnostics of vanadium dioxide thin films. *Thin Solid Films* **204**, L1-L4 (1991).
35. C. S. Tang, et al. Interfacial Oxygen-Driven Charge Localization and Plasmon Excitation in Unconventional Superconductors. *Adv Mater* **32**, 2000153 (2020).
36. C. S. Tang, et al. Anisotropic Collective Charge Excitations in Quasimetallic 2D Transition-Metal Dichalcogenides. *Adv Sci* **7**, 1902726 (2020).
37. X. Yin, et al. Quantum Correlated Plasmons and Their Tunability in Undoped and Doped Mott-Insulator Cuprates. *ACS Photonics* **6**, 3281-3289 (2019).

38. N. Nucker, et al. Plasmons and interband transitions in Bi₂Sr₂CaCu₂O₈. *Phys Rev B Condens Matter* **39**, 12379-12382 (1989).
39. A. Bianconi, S. Stizza&R. Bernardini Critical behavior of the plasmon resonance at the metal-insulator transition in VO₂. *Phys. Rev. B* **24**, 4406-4411 (1981).
40. S. Uchida, et al. Optical spectra of La_{2-x}Sr_xCuO₄: Effect of carrier doping on the electronic structure of the CuO₂ plane. *Phys Rev B Condens Matter* **43**, 7942-7954 (1991).
41. J. B. Kana Kana, G. Vignaud, A. Gibaud&M. Maaza Thermally driven sign switch of static dielectric constant of VO₂ thin film. *Opt. Mater* **54**, 165-169 (2016).
42. T. C. Asmara, et al. Tunable and low-loss correlated plasmons in Mott-like insulating oxides. *Nat Commun* **8**, 15271 (2017).
43. H. Gao, et al. Ultra-flat and long-lived plasmons in a strongly correlated oxide. *Nat Commun* **13**, 4662 (2022).
44. H.-K. Jin&J. Knolle Flat and correlated plasmon bands in graphene/ α -RuCl₃ heterostructures. *Physical Review B* **104**, (2021).
45. T. J. Whitcher, et al. Correlated plasmons in the topological insulator Bi₂Se₃ induced by long-range electron correlations. *NPG Asia Materials* **12**, (2020).
46. T. J. Smart, T. A. Pham, Y. Ping&T. Ogitsu Optical absorption induced by small polaron formation in transition metal oxides: The case of Co₃O₄. *Phys. Rev. Mater* **3**, 102401(R) (2019).
47. L. R. De Jesus, et al. Mapping polaronic states and lithiation gradients in individual V₂O₅ nanowires. *Nat Commun* **7**, 12022 (2016).
48. A. Chaudhuri, et al. Direct observation of anisotropic small-hole polarons in an orthorhombic structure of BiVO₄ films. *Phys. Rev. B* **97**, 195150 (2018).
49. C. Franchini, M. Reticcioli, M. Setvin&U. Diebold Polarons in materials. *Nat Rev Mater* **6**, 560-586 (2021).
50. C. A. Triana, C. G. Granqvist&G. A. Niklasson Electrochromism and small-polaron hopping in oxygen deficient and lithium intercalated amorphous tungsten oxide films. *Journal of Applied Physics* **118**, 024901 (2015).
51. C. A. Triana, C. G. Granqvist&G. A. Niklasson Optical absorption and small-polaron hopping in oxygen deficient and lithium-ion-intercalated amorphous titanium oxide films. *Journal of Applied Physics* **119**, 015701 (2016).
52. D. Emin Optical properties of large and small polarons and bipolarons. *Phys Rev B Condens Matter* **48**, 13691-13702 (1993).
53. V. V. Bryksin Small-polaron theory with allowance for the influence of lattice vibrations on the resonance integral. *Journal of Experimental and Theoretical Physics* **73**, 861-866 (1991).
54. V. S. Vikhnin, S. Lysenko, A. Rua, F. Fernandez&H. Liu Charge transfer model of metal-insulator phase transition and ultrafast optical response in VO₂. *Optical Materials* **29**, 1385-1389 (2007).
55. J. S. Ulla Gro Nielsen, Hans J. Jakobsen β -VO₂- a V(IV) or a mixed-valence V(III)-V(V)oxide - studied by 51V MAS NMR spectroscopy. *Chem. Phys. Lett* **356**, 73-78 (2002).

56. D. Wickramaratne, N. Bernstein&I. I. Mazin Role of defects in the metal-insulator transition in VO₂ and V₂O₃. *Phys. Rev. B* **99**, 214103 (2019).
57. S. Joshi, N. Smieszek&V. Chakrapani Effects of charge fluctuation and charge regulation on the phase transitions in stoichiometric VO₂. *Sci. Rep* **10**, 17121 (2020).
58. C. Chen&Z. Fan Changes in VO₂ band structure induced by charge localization and surface segregation. *Appl. Phys. Lett* **95**, 262106 (2009).
59. C. Wu, et al. Direct hydrothermal synthesis of monoclinic VO₂(M) single-domain nanorods on large scale displaying magnetocaloric effect. *J. Mater. Chem* **21**, 4509 (2011).
60. M. Nakano, et al. Collective bulk carrier delocalization driven by electrostatic surface charge accumulation. *Nature* **487**, 459-62 (2012).
61. C. Chen, et al. Influence of defects on structural and electrical properties of VO₂ thin films. *J. Appl. Phys* **110**, 023707 (2011).
62. N. F. Mott Metal-Insulator Transition. *Rev. Mod. Phys.* **40**, 677-683 (1968).
63. X. Zhong, P. LeClair, S. K. Sarker&A. Gupta Metal-insulator transition in epitaxial VO₂ thin films on TiO₂(100). *Phys. Rev. B* **86**, 094114 (2012).
64. V. N. Andreev&V. A. Klimov Electrical conductivity of the semiconducting phase in vanadium dioxide single crystals. *Phys. Solid State* **49**, 2251-2255 (2007).
65. D. Ruzmetov, S. D. Senanayake&S. Ramanathan X-ray absorption spectroscopy of vanadium dioxide thin films across the phase-transition boundary. *Physical Review B* **75**, 195102 (2007).
66. T. C. Koethe, et al. Transfer of spectral weight and symmetry across the metal-insulator transition in VO₂. *Phys Rev Lett* **97**, 116402 (2006).
67. N. F. Quackenbush, et al. Stability of the M2 phase of vanadium dioxide induced by coherent epitaxial strain. *Physical Review B* **94**, 085105 (2016).
68. D. K. S. Suhail Majid, F Rahman, Kamini Gautam, V G Sathe, R J Choudhary and D M Phase Characterization of pulsed laser deposition grown V₂O₃ converted VO₂. *Journal of Physics: Conference Series* **755**, 012027 (2016).
69. G. Kresse&J. Hafner Ab initio molecular dynamics for liquid metals. *Phys. Rev. B* **47**, 558-561 (1993).
70. G. Kresse&J. Hafner Ab initio molecular dynamics for open-shell transition metals. *Phys. Rev. B* **48**, 13115-13118 (1993).
71. P. E. Blöchl Projector augmented-wave method. *Phys. Rev. B* **50**, 17953-17979 (1994).
72. J. P. Perdew, K. Burke&M. Ernzerhof Generalized Gradient Approximation Made Simple. *Phys. Rev. Lett.* **77**, 3865-3868 (1996).
73. S. L. Dudarev, G. A. Botton, S. Y. Savrasov, C. J. Humphreys&A. P. Sutton Electron-energy-loss spectra and the structural stability of nickel oxide: An LSDA+U study. *Phys. Rev. B* **57**, 1505-1509 (1998).
74. T. Yang, et al. Structural Reconstruction Modulated Physical Properties of Titanium Oxide at the Monolayer Limit. *J. Phys. Chem. C* **127**, 5631-5639 (2023).
75. W. Kong, et al. Formation of two-dimensional small polarons at the conducting LaAlO₃/SrTiO₃ interface. *Phys. Rev. B* **100**, 085413 (2019).

76. A. Chaudhuri, et al. Direct observation of anisotropic small-hole polarons in an orthorhombic structure of BiVO₄ films. *Phys. Rev. B* **97**, 195150 (2018).
77. J. Kaur, M. L. H. Chandrappa, C. Chen & S. P. Ong Polaron-induced metal-to-insulator transition in vanadium oxides from density functional theory calculations. *Physical Review B* **107**, 125162 (2023).
78. S. Cheng, et al. Inherent stochasticity during insulator–metal transition in VO₂. *Proceedings of the National Academy of Sciences* **118**, e2105895118 (2021).
79. W. Kong, et al. Tunable Rashba spin-orbit coupling and its interplay with multi-orbital effect and magnetic ordering at oxide interfaces. *Physical Review B* **104**, 155152 (2021).
80. M. Setvin, et al. Direct View at Excess Electrons in TiO₂ Rutile and Anatase. *Phys. Rev. Lett.* **113**, 086402 (2014).
81. M. Reticcioli, et al. Interplay between Adsorbates and Polarons: CO on Rutile TiO₂(110). *Phys. Rev. Lett.* **122**, 016805 (2019).
82. M. Reticcioli, et al. Polaron-Driven Surface Reconstructions. *Phys. Rev. X* **7**, 031053 (2017).
83. Z. Zhu & U. Schwingenschlögl Comprehensive picture of VO₂ from band theory. *Phys. Rev. B* **86**, 075149 (2012).